Stability and Control Analysis of a Rudderless Aircraft with Rotary Horizontal Tail

Jarrett Theodore Van Dyke

A thesis
submitted in partial fulfillment of the
requirements for the degree of

Master of Science

University of Washington

2024

Committee:
Dana Dabiri
Mehran Mesbahi

Program Authorized to Offer Degree:
William E. Boeing Department of Aeronautics and Astronautics

University of Washington

Abstract

Stability and Control Analysis of a Rudderless Aircraft with Rotary Horizontal Tail

Jarrett Theodore Van Dyke

Chair of the Supervisory Committee:
Dana Dabiri
William E. Boeing Department of Aeronautics and Astronautics

Removing the vertical tail on an aircraft has the potential to significantly increase efficiency and range. However, in conventional configurations the vertical tail provides essential lateral and directional stability. A solution to this loss of stability is a rotary horizontal tail, whereby the horizontal tail rotates to provide yaw moments to stabilize the aircraft. This technique is similar to how some birds rotate their tails to induce rolling and yawing moments. This study sought to determine the feasibility of controlling a standard aircraft modified with a rotary horizontal tail by modeling an aircraft similar to a Cessna 172. First, an aerodynamic analysis using a vortex lattice method solver was completed to determine the drag reduction benefits of the modification. Then, a static and dynamic stability analysis was conducted to assess the impact of the modification. Last, three feedback controllers were designed and applied to stabilize and control both the conventional and modified aircraft, and the performance and robustness qualities of each were compared. The first controller was an optimal state-feedback linear quadratic regulator. It was found that this controller design resulted in similar time-domain performance between configurations, but the robustness of the modified model, characterized by the closed-loop transfer matrix, sensitivity functions, and direct perturbation, was significantly degraded compared to the conventional model. The second and third controllers were a state-feedback guaranteed-cost design, which resulted in nearly equivalent robustness between the two configurations. However, the time-domain performance of the modified system was found to be degraded compared to the conventional system. Therefore, from this study we are able to conclude that it is feasible to stabilize and control an aircraft with a rotary horizontal tail configuration, but there will likely be a greater trade-off between performance and robustness compared to a conventional aircraft.

TABLE OF CONTENTS

LIST OF FIGURES

Figure Number Page

LIST OF TABLES

ACKNOWLEDGMENTS

I would like to thank my advisors Professor Dana Dabiri and Professor Mehran Mesbahi for the opportunity to work on this project and for their help and guidance. I would also like to thank Eddie Ting for his help along the way.

I am grateful for my fiancé, and for my parents; for their support, dedication, love, and encouragement throughout this process. Most importantly, I am grateful to God, without whom I could do nothing. "For from Him and through Him and to Him are all things. To Him be the glory forever. Amen." (Romans 11:36)

Disclaimer Clause

The views expressed in this thesis are those of the author and do not reflect the official policy or position of the United States Air Force, Department of Defense, or the U.S. Government.

Chapter 1

INTRODUCTION

Conventional aircraft design requires separate vertical and horizontal control surfaces to provide stability and control in the longitudinal, lateral, and directional axes. However, this stability comes at the cost of range, since these surfaces can add significantly to the overall drag. Some designs have attempted to reduce this drag through combination of the vertical and horizontal tails into a ”V-tail”, such as in the Northrop YF-23. Another option is the flying wing design, such as the Northrop Grumman B-2 Spirit, which eliminates the vertical tail entirely, utilizing its wide, swept wings to maintain stability. Still another option is replacing the tail with thrust vectoring, such as in the McDonnell Douglas X-36.

An unconventional approach to this problem is to replace the typical empennage with a rotary horizontal tail, as shown in Figure 1.1 [35]. This configuration may reduce drag through elimination of the vertical surface while maintaining control authority through rotation of the horizontal tail. It has been theorized that birds similarly maintain control and stability through rotating their tails [18]. Figure 1.2 shows a golden eagle in flight with its tail clearly rotated. This image was taken from a video, which shows how its tail rotates often to provide stabilization in soaring flight [21].

While eliminating the vertical tail may result in drag and weight reduction, it could pose significant stability challenges. On a conventional aircraft, the vertical tail provides nearly all of the directional stability and part of the lateral stability [38]. This loss of stability would make the aircraft very difficult for a human pilot to fly. Thus, a digital control system is likely needed to stabilize an aircraft with a rotary horizontal tail.

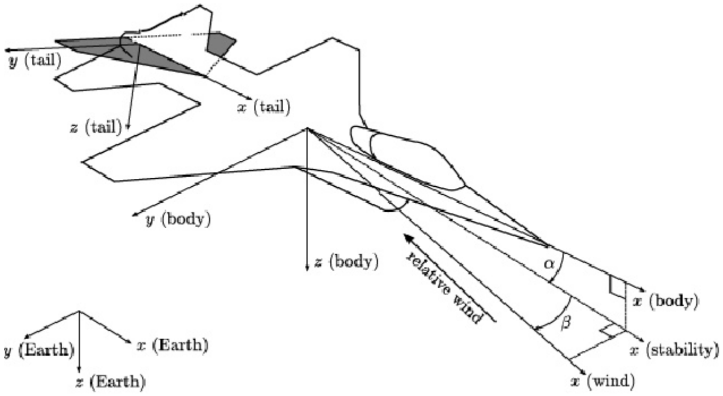

Figure 1.1: Diagram showing axes systems for an aircraft with a rotary horizontal tail

Figure 1.2: Golden eagle in flight showing tail rotation, adapted from [21]

1.1 Literature Review

The configuration of a rotary horizontal tail has been explored recently under the name "Bio-Inspired Rotating Empennage (BIRE)" at Utah State University in cooperation with the Air Force Research Laboratory, where it has been applied to an aircraft similar to the F-16 [4]. An aerodynamic model was developed and the static trim of the modified aircraft was compared to the baseline. It was found that the BIRE system could replicate the trim conditions of the baseline, but that tail strike was a possible concern when landing in steady-heading sideslip [4]. Furthermore, a linearized rigid-body model of the BIRE aircraft was created and the static and dynamic stability analyzed. It was found that the BIRE decreased the static stability in all axes and worsened the dynamic stability for all modes. More interestingly, the BIRE modification produced a non-traditional, non-oscillatory Dutch roll mode, for which the physical representation could not be deduced [20]. Most recently, this rigid-body model of the BIRE aircraft, along with added first-order actuator models, was used to design an infinite-horizon linear quadratic regulator [24]. This study found that the BIRE system was controllable and robust to single-variable model errors and gusts. They also found that the tail rotation and throttle input were used little in simulations and the system remained controllable if these inputs were eliminated from the linearized system.

At the University of Washington, the rotary horizontal tail configuration was originally explored and compared to other configurations in wind tunnel tests. Figure 1.3 shows some lift-to-drag ratio results of these tests, which promised the possibility of significant increases in aerodynamic efficiency. Later vortex lattice method computations supported these findings and found that the rotary horizontal tail configuration reduced the total drag coefficient by an average of 3.18% in steady level flight and 10.4% for certain control surface deflection angles. Similar to the BIRE analysis, the Dutch roll mode was found to be non-traditional and non-oscillatory. However, the linear system was found to be controllable [35].

In 2007, a similar rotary tail configuration was explored with a micro air vehicle. The V-tail on a small UAV was replaced with a mostly flat tail that could rotate and pivot

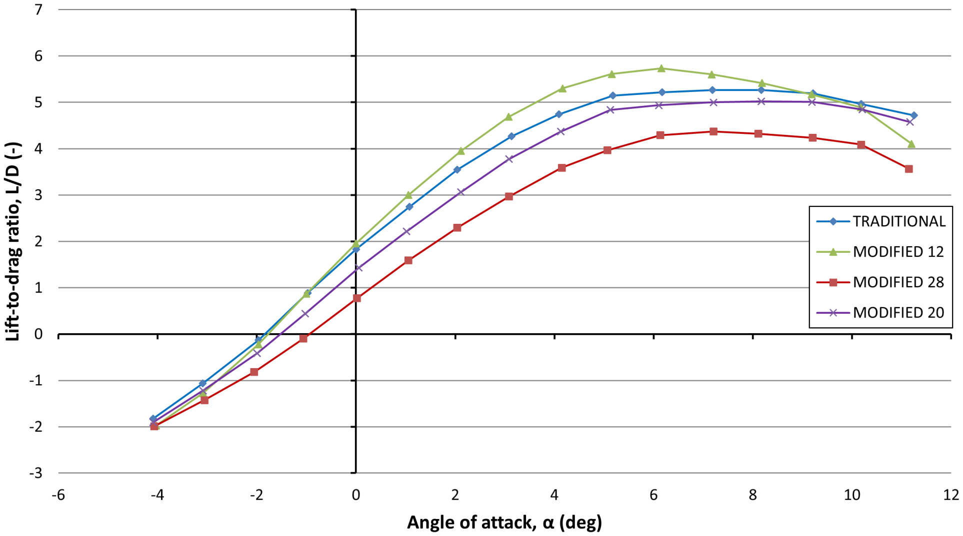

Figure 1.3: University of Washington exploratory wind tunnel data

about the joint with the fuselage, and wind tunnel tests were done to determine the forces and moments it generated. The study found that the rotating tail could generate a level of control comparable to that of a typical rudder control configuration, with the added benefit of the ability to use the tail as an air brake. However, the controls were highly coupled, which would make it difficult for a human to fly [26].

Chapter 2

THEORY

2.1 Computational Aerodynamics

The computational aerodynamics software used in this effort was Athena Vortex Lattice (AVL) and xflr5. AVL relies exclusively on the vortex lattice method (VLM), while xflr5 combines VLM with one- and two-dimensional empirical and theoretical turbulence and transition models [15][8].

Vortex lattice methods are solutions to Laplace's equations and thus are a result of an inviscid estimation of the Navier-Stokes equations, as shown in Figure 2.1 [8]. Laplace's equations are derived from potential flow theory, which are derived from the Euler equations. Thus, vortex lattice method assumes inviscid, irrotational, incompressible flow with uniform onset flow [7]. In AVL and xflr5, lifting surfaces and their trailing wakes are represented as single-layer vortex sheets which are discretized into horseshoe vortex filaments. Quasi-steady flow is also assumed, meaning that unsteady vortex shedding is ignored. In AVL, compressibility is reintroduced using the Prandtl-Glauert correction [15].

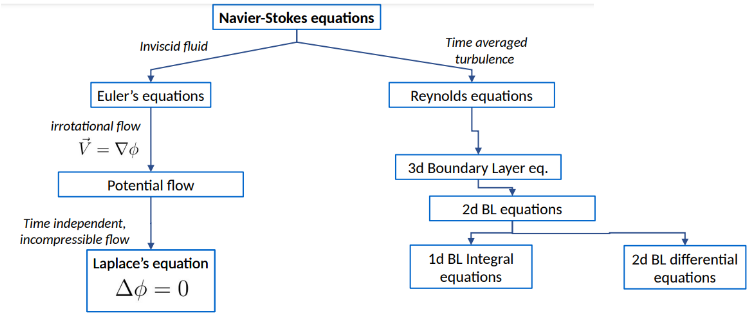

Figure 2.1: Relationship of the various types of computational aerodynamics

2.2 Aircraft Stability

Aircraft stability can be divided into two regimes: static and dynamic. Static stability refers to the initial tendency of the aircraft after being perturbed from the trim condition, while dynamic stability is the behavior of the aircraft over time due to a perturbation. The moments, velocities, and derivatives for stability are based on the stability axis shown in Figure 1.1, where l, m, and n denote the moments about the x, y, and z axes, respectively.

The static stability characteristics are described by the derivatives of the moment coefficients with respect to angle of attack or sideslip angle about the trim condition. Positive static stability is defined as an aircraft's initial tendency to return to the trim condition after a perturbation. Neutrally stable aircraft will effectively establish a new trim condition. Negatively stable aircraft tend to exacerbate the perturbation.

Longitudinal static stability refers to the aircraft's response in the longitudinal direction, defined by the angle of attack (α). For positive static stability, the change in pitching moment coefficient (C_m) with angle of attack must be negative ($C_{m_\alpha} = \frac{\delta C_m}{\delta \alpha} < 0$), as shown in Fig. 2.2a. Lateral static stability refers to the aircraft's response in the lateral direction, defined by the sideslip angle (β). To maintain wings level flight after a perturbation, the change in rolling moment coefficient (C_l) with sideslip angle must be negative ($C_{l_\beta} = \frac{\delta C_l}{\delta \beta} < 0$), as shown in Fig. 2.2b. Directional static stability refers to the aircraft's response to reduced the sideslip angle (β) after a perturbation. For positive directional stability, the change in yawing moment coefficient (C_n) with sideslip angle must be positive ($C_{n_\beta} = \frac{\delta C_n}{\delta \beta} > 0$), as seen in Fig. 2.2c [38].

While static stability describes the initial tendency of the system, dynamic stability describes the behavior of the system over time. A dynamically stable system will return to trim over time, while a dynamically unstable system will depart from trim over time, regardless of the static stability. If the system is statically stable, after a perturbation it may overshoot the original trim point and oscillate about it. If it is dynamically stable, those oscillations will dampen over time, but if it is dynamically unstable, the amplitude will

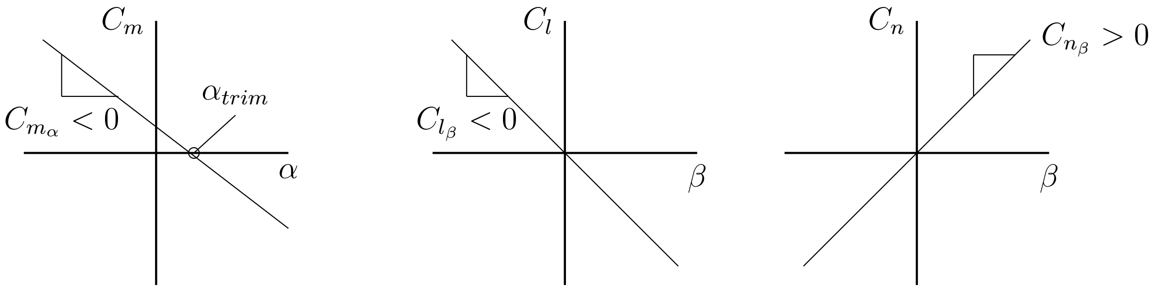

(a) Pitching moment (b) Rolling moment (c) Yawing moment

Figure 2.2: Typical aircraft static stability derivatives

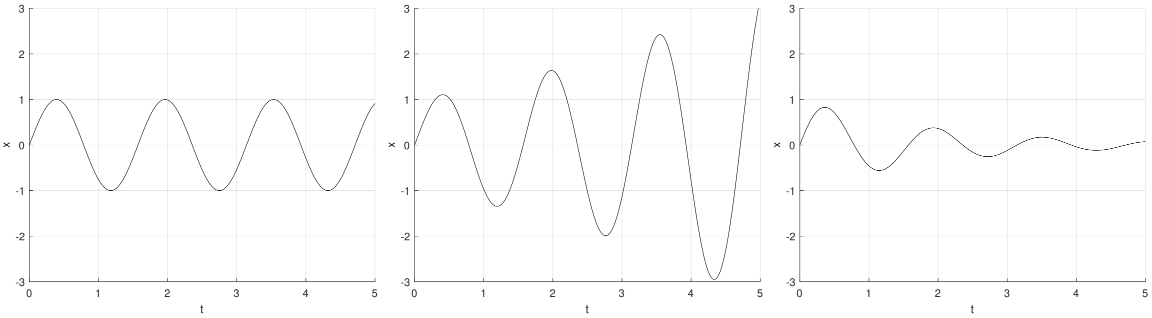

(a) Neutral stability (b) Negative stability (c) Positive stability

Figure 2.3: Examples of dynamic stability types with positive static stability

grow and the aircraft will depart stable flight if left unchecked. Aircraft have five standard dynamic modes: short period, phugoid, Dutch roll, roll subsidence, and spiral mode.

The short period mode is an oscillatory longitudinal mode excited by pitch perturbations. It is characterized by oscillations in the angle of attack and pitch angle, while altitude and airspeed remain relatively constant. The short period is typically highly damped and high frequency, and therefore lasts only a few seconds.

The phugoid mode is also an oscillatory longitudinal mode excited by pitch perturbations. However, unlike the short period, the oscillations occur mainly in the airspeed and altitude of the aircraft while the angle of attack remains relatively constant. The phugoid is lightly damped and low frequency and thus can last for several minutes if not corrected.

The Dutch roll mode is an oscillatory lateral-directional mode excited by roll and yaw perturbations. In the Dutch roll mode, the roll and yaw angles oscillate in a coupled fashion. The degree to which the oscillations are in the roll or yaw axis is determined by the absolute value of the ratio between the roll and yaw static stability derivatives ($|C_{l_\beta}/C_{n_\beta}|$). The greater this ratio, the more the oscillations occur in the yaw angle and the less they occur in the roll angle. This mode is moderately damped and fairly high frequency, typically persisting for tens of seconds.

The roll mode is a non-oscillatory lateral mode. It is essentially the resistance of the aircraft to roll rates.

The spiral mode is a non-oscillatory directional mode. It is the tendency of the aircraft to enter a spiral dive due to a roll angle perturbation. In most conventional aircraft, the spiral mode is unstable.

2.3 Aircraft Simulation

2.3.1 Reference Frames

Convention defines four main frames of reference for describing aircraft in space: inertial, body, stability, and wind frames. The inertial frame is Earth-fixed where the x-axis points north, the y-axis points east, and the z-axis points down. This frame is useful for navigation and the origin can be positioned anywhere. The body frame is centered on the aircraft such that the x-axis points out the nose, the y-axis is orthogonal and points out the right wing, and the z-axis is orthogonal to both and points out the bottom of the aircraft. The relationship between the orientation of the inertial and body frames are described by the Euler angles ϕ, θ, and ψ, which are the rotation angles about the x, y, and z axes, respectively. The stability frame is identical to the body frame except that it is rotated about the y-axis by the angle of attack (α) such that the x-axis is aligned with the relative wind if there is no sideslip. Similarly, the wind axis is the stability axis rotated about the z-axis by the sideslip angle (β) such that the relative wind is always aligned with the x-axis. All of these reference frames are shown in Figure 1.1.

Transformation from one frame to another can be accomplished by multiplying the position vector by a series of rotation matrices. To go from the inertial frame to the body frame, the position vector is first multiplied by the rotation matrix shown in Eqn 2.1 to rotate the frame about the z-axis, then by the rotation matrix in Eqn 2.2 to rotate about the y-axis, then by the matrix in Eqn 2.3 to rotate about the x-axis. The combination of this entire transformation is called the Direction Cosine Matrix (DCM) and is shown in Eqn 2.4.

$$C_{1/v} = \begin{bmatrix} \cos\psi & \sin\psi & 0 \\ -\sin\psi & \cos\psi & 0 \\ 0 & 0 & 1 \end{bmatrix} \tag{2.1}$$

$$C_{2/1} = \begin{bmatrix} \cos\theta & 0 & -\sin\theta \\ 0 & 1 & 0 \\ \sin\theta & 0 & \cos\theta \end{bmatrix} \tag{2.2}$$

$$C_{b/2} = \begin{bmatrix} 1 & 0 & 0 \\ 0 & \cos\phi & \sin\phi \\ 0 & -\sin\phi & \cos\phi \end{bmatrix} \tag{2.3}$$

$$C_{b/v} = C_{b/2}C_{2/1}C_{1/v} = \begin{bmatrix} \cos\theta\cos\psi & \cos\theta\sin\psi & -\sin\theta \\ -\cos\phi\sin\psi+\sin\phi\sin\theta\cos\psi & \cos\phi\cos\psi+\sin\phi\sin\theta\sin\psi & \sin\phi\cos\theta \\ \sin\phi\sin\psi+\cos\phi\sin\theta\cos\psi & -\sin\phi\cos\psi+\cos\phi\sin\theta\sin\psi & \cos\phi\cos\theta \end{bmatrix} \tag{2.4}$$

Transformation from the body frame to the stability frame is performed through rotation through the angle of attack by multiplication by the rotation matrix shown in Eqn 2.5. Similarly, transformation from the stability frame to the wind frame is a rotation through the sideslip angle by multiplication by the rotation matrix in Eqn 2.6. The total rotation matrix from the body frame to the wind frame is given in Eqn 2.7 [34].

$$C_{s/b} = \begin{bmatrix} \cos\alpha & 0 & \sin\alpha \\ 0 & 1 & 0 \\ -\sin\alpha & 0 & \cos\alpha \end{bmatrix} \tag{2.5}$$

$$C_{w/s} = \begin{bmatrix} \cos\beta & \sin\beta & 0 \\ -\sin\beta & \cos\beta & 0 \\ 0 & 0 & 1 \end{bmatrix} \tag{2.6}$$

$$C_{w/b} = C_{s/b}C_{w/s} = \begin{bmatrix} \cos\alpha\cos\beta & \sin\beta & \sin\alpha\cos\beta \\ -\cos\alpha\sin\beta & \cos\beta & -\sin\alpha\sin\beta \\ -\sin\alpha & 0 & \cos\alpha \end{bmatrix} \tag{2.7}$$

2.3.2 Equations of Motion

Aircraft simulation involves using the aerodynamic, propulsive, and gravitational forces and moments to determine the dynamic response. This is done through a set of nonlinear state-space equations, such that $\dot{x} = f(x, u)$, where x is the state vector and u is the control input vector. The first three states are the translational velocities, $\bar{V}^b = [u, v, w]$, in the body frame x, y, and z axes, respectively. Assuming the Earth is flat and not rotating, and the vehicle-carried inertial frame is not rotating, Newton's 2nd Law gives Eqn 2.9. The Coriolis equation, found in Eqn 2.10, allows the acceleration in the inertial frame to be calculated from the acceleration in the body frame and known body frame states. This substitution results in the translational equation of motion shown in Eqn 2.11.

$$\bar{F}^b = m\dot{V}^i \tag{2.8}$$

$$\dot{\bar{V}}^i = \dot{\bar{V}}^b + \bar{\omega}^b \times \bar{V} \tag{2.9}$$

$$\dot{\bar{V}}^b = \frac{1}{m}\bar{F}^b - \bar{\omega}^b \times \bar{V}^b \tag{2.10}$$

$$\begin{bmatrix} \dot{u} \\ \dot{v} \\ \dot{w} \end{bmatrix} = \frac{1}{m}\bar{F}^b - \begin{bmatrix} p \\ q \\ r \end{bmatrix} \times \begin{bmatrix} u \\ v \\ w \end{bmatrix} \tag{2.11}$$

The next three states are the rotational velocities, $\bar{\omega}^b = [p, q, r]$. The derivation of the rotational equations of motion is similar to the translational derivation, where mass is now the moment of inertia (I_b) and forces are moments. Newton's 2nd Law and the Coriolis equation gives Eqn 2.13. Assuming that the moment of inertia does not change with time results in Eqn 2.14. Solving for the rotational acceleration in the body axis, the rotational equations of motion are given in Eqn 2.16.

$$\bar{M}^b = \frac{d}{dt}(I_b\bar{\omega}^b) + \bar{\omega}^b \times I_b\bar{\omega}^b \tag{2.12}$$

$$\bar{M}^b = I_b\dot{\bar{\omega}}^b + \bar{\omega}^b \times I_b\bar{\omega}^b \tag{2.13}$$

$$\dot{\bar{\omega}}^b = I_b^{-1}\left(\bar{M}^b - \bar{\omega}^b \times I_b\bar{\omega}^b\right) \tag{2.14}$$

$$\begin{bmatrix} \dot{p} \\ \dot{q} \\ \dot{r} \end{bmatrix} = I_b^{-1}\left(\begin{bmatrix} L \\ M \\ N \end{bmatrix} - \begin{bmatrix} p \\ q \\ r \end{bmatrix} \times I_b \begin{bmatrix} p \\ q \\ r \end{bmatrix}\right) \tag{2.15}$$

$$\tag{2.16}$$

The next six states are the rotational and translational positions. The rates of change of these positions are simply tranformations into the inertial frame of the body frame rates, which are the first six states. Therefore, the rotational position equations of motion are given in Eqn 2.18 and the translational position equations of motion, or navigation equations, are given in Eqn 2.19.

$$H(\Phi) = \begin{bmatrix} 1 & \tan\theta\sin\phi & \tan\theta\cos\phi \\ 0 & \cos\phi & -\sin\phi \\ 0 & \sin\phi/\cos\theta & \cos\phi/\cos\theta \end{bmatrix} \tag{2.17}$$

$$\dot{\Phi} = \begin{bmatrix} \dot{\phi} \\ \dot{\theta} \\ \dot{\psi} \end{bmatrix} = H(\Phi)\bar{\omega}^b \tag{2.18}$$

$$\dot{\bar{V}}^v = \begin{bmatrix} \dot{P}_N \\ \dot{P}_E \\ \dot{P}_D \end{bmatrix} = C_{v/b}(\Phi)\bar{V}^b = C_{b/v}^{-1}(\Phi) \begin{bmatrix} u \\ v \\ w \end{bmatrix} \tag{2.19}$$

2.4 Linear Control Theory

2.4.1 Linearization

Real-world systems are almost always nonlinear and can be characterized by the equation $\dot{x} = f(x,u)$. A linear system takes the form in Eqn 2.20, where x is the n-dimensional state vector and u is the m-dimensional input vector.

$$\begin{aligned} \dot{x} &= Ax + Bu \\ y &= Cx + Du \end{aligned} \tag{2.20}$$

One method of linearizing a nonlinear system is through Taylor series expansion, the result of which is found in Eqn 2.21.

$$\begin{aligned} \Delta\dot{x} &= A\Delta x + B\Delta u \\ \text{where} \quad A &= -E^{-1}A' \; ; \; B = -E^{-1}B' \end{aligned} \tag{2.21}$$

The Jacobian matrices E, A', and B' are defined in Eqns 2.22, 2.23, and 2.24, respectively. The elements of these matrices can be calculated numerically through the symmetric difference quotient, an example of which is shown in Eqn 2.25

$$E = \begin{bmatrix} \frac{\partial F_1}{\partial \dot{x}_1} & \cdots & \frac{\partial F_1}{\partial \dot{x}_n} \\ \vdots & \ddots & \vdots \\ \frac{\partial F_n}{\partial \dot{x}_1} & \cdots & \frac{\partial F_n}{\partial \dot{x}_n} \end{bmatrix} \tag{2.22}$$

$$A' = \begin{bmatrix} \frac{\partial F_1}{\partial x_1} & \cdots & \frac{\partial F_1}{\partial x_n} \\ \vdots & \ddots & \vdots \\ \frac{\partial F_n}{\partial x_1} & \cdots & \frac{\partial F_n}{\partial x_n} \end{bmatrix} \tag{2.23}$$

$$B' = \begin{bmatrix} \frac{\partial F_1}{\partial u_1} & \cdots & \frac{\partial F_1}{\partial u_n} \\ \vdots & \ddots & \vdots \\ \frac{\partial F_n}{\partial u_1} & \cdots & \frac{\partial F_n}{\partial u_n} \end{bmatrix} \tag{2.24}$$

$$A'_{i,j} = \frac{\partial F_i}{\partial x_j} = \frac{F_i(\dot{x}_0, x_{i,j+}, u_0) - F_i(\dot{x}_0, x_{i,j-}, u_0)}{2\Delta x_{i,j}} \tag{2.25}$$

$$x_{i,j+} = \begin{bmatrix} x_1 & \dots & x_j + \Delta x_{i,j} & \dots & x_n \end{bmatrix}^T \tag{2.26}$$

2.4.2 Linear Systems

The stability of a linear system of the form shown in Eqn 2.20 is characterized by the eigenvalues of the A-matrix, also known as the poles of the system. If the eigenvalues are purely real, then the mode is non-oscillatory, while poles with imaginary parts are oscillatory. The stability of the mode depends on the sign of the real part of the associated eigenvalue: a negative real part indicates the mode is stable, while a positive real part indicates an unstable mode.

A system is controllable if it is able to be driven from any initial state to any final state in some finite time. The controllability of a system is characterized by the controllability matrix shown in Eqn 2.27 and the system is controllable if and only if $\text{rank}(\mathcal{C}) = n$, where $A \in \mathcal{R}^{n \times n}$, $B \in \mathcal{R}^{n \times m}$.

$$\mathcal{C} = [B \quad AB \quad A^2B \quad \dots \quad A^{n-1}B] \tag{2.27}$$

A more lenient condition is stabilizability, which is the condition that there exists a gain K such that all of the poles of the system $A+BK$ are stable. The pair (A, B) is stabilizable if and only if $\text{rank}[A - \lambda I \quad B] = n$ for every eigenvalue λ of A with a non-negative real part.

Similarly, an observable system is one whose state history can be determined from its inputs and outputs. The observability matrix is defined in Eqn 2.28 and a system is observable if and only if $\text{rank}(\mathcal{O}) = n$.

$$\mathcal{O} = \begin{bmatrix} C \\ CA \\ CA^2 \\ \vdots \\ CA^{n-1} \end{bmatrix} \tag{2.28}$$

Similar to stabilizability, a more lenient condition is detectability. The pair (A, C) is detectable if and only if rank $\begin{bmatrix} A - \lambda I \\ C \end{bmatrix} = n$ for every eigenvalue λ of A with a non-negative real part. [12]

2.4.3 Robust Control

In reality, the true plant model is never certain. Because of this uncertainty, it is important that the controlled system maintains stability if there are perturbations to the system. This quality is referred to as the robustness of the system. Robustness can be divided into two types: stability and performance. Stability robustness is the ability of the system to remain stable even in the event of modeling errors. Performance robustness is the ability to guarantee performance even if the system is subject to disturbances such as wind gusts and sensor noise [34]. A typical block diagram of a feedback-controlled system is shown in Figure 2.4.

For SISO systems, the robustness can be characterized by the gain and phase margins. For MIMO systems, the robustness can be characterized by the singular values of the loop transfer function matrix, the sensitivity function, and the complementary sensitivity (cosensitivity) function. The output and input loop transfer functions are defined in Equations 2.29 and 2.30, respectively. The sensitivity functions are defined in Equations 2.31 and 2.34 and the cosensitivity functions in Equations 2.32 and 2.35 [31]. For good performance robustness, the minimum singular value of $L(j\omega)$ should be large at low frequencies and the maximum singular value should be small at high frequencies. For good stability robustness, the maximum singular value of $L(j\omega)$ should be small at low frequencies to guard against model parameter variations and small at high frequencies to guard against unmodelled high-frequency dynamics. Likewise, for good disturbance rejection the sensitivity function should be small at low frequencies and for good sensor noise rejection the cosensitivity function should be small at high frequencies. [34]

$$L_o = GK \tag{2.29}$$

$$L_i = KG \tag{2.30}$$

$$S_o = (I + GK)^{-1} \tag{2.31}$$

$$T_o = (I + GK)^{-1}GK \tag{2.32}$$

$$S + T = I \tag{2.33}$$

$$S_i = (I + KG)^{-1} \tag{2.34}$$

$$T_i = (I + KG)^{-1}KG \tag{2.35}$$

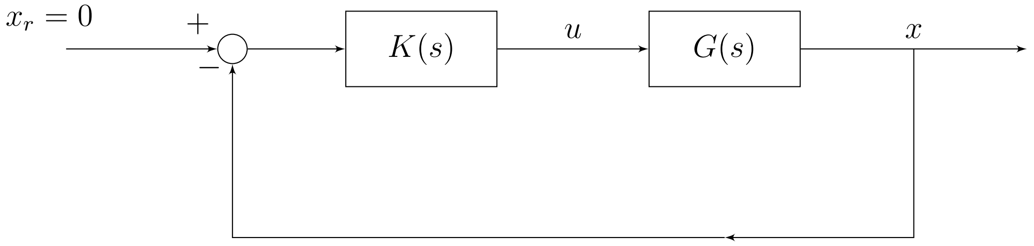

Figure 2.4: Standard state-feedback block diagram configuration

2.5 Controller Design

2.5.1 Linear Quadratic Regulator

The linear quadratic regulator (LQR) is a method for designing the optimal state-feedback control law in the form $u = -Kx$. This is given by minimizing a performance measure in the form shown in Eqn 2.36 [12].

$$V = \int_0^T (x^T Q x + u^T R u) dt + x^T(T) M x(T) \tag{2.36}$$

In this problem, Q and M are positive semidefinite matrices and R is a positive definite matrix. Q is the weighting matrix for the states and R is the weighting matrix for the controls, allowing the designer to penalize more heavily deviations in certain states and controls. M is the final state weighting matrix, which is zero for infinite horizon problems. The optimal state-feedback gain for continuous time is given by solving the continuous algebraic Riccati equation (CARE), shown in Eqn 2.37. The optimal control is thus given by Eqn 2.38.

$$0 = A^T P + PA + Q - PBR^{-1}B^T P \tag{2.37}$$

$$u^*(t) = -R^{-1}B^T P x(t) \tag{2.38}$$

There always exists a constant control law of this form if the system is controllable or stabilizable.

LQR state-feedback controlled systems have built-in robustness qualities quite by accident, since robustness was not in the original formulation of LQR theory [12]. According to Kalman's Inequality, we know that for LQR full-state-feedback, Eqn 2.39 holds.

$$\underline{\sigma}(I + H(j\omega)) \geq 1, \quad \forall\omega \tag{2.39}$$

2.5.2 Guaranteed-Cost Design

One method to design a controller to guarantee the robustness of a system with respect to A-matrix perturbations is the guaranteed-cost method. This method designs a controller that guarantees system stability for some ΔA such that $\dot{x} = (A + \Delta A)x + Bu$. The perturbations are defined according to Eqn 2.40, where A_i contains the absolute maximum perturbations to specified entries of A and adheres to the normalized bounding condition $|w_i| \leq 1$.

$$\Delta A = \sum_{0}^{q} w_i A_i = \sum_{0}^{q} w_i D_i E_i \tag{2.40}$$

Controller design is accomplished by solving the algebraic Riccati equation, just as in LQR, but with an additional bounding term, shown in Eqn 2.41.

$$0 = A^T P + PA + Q - PBR^{-1}B^T P + \mathcal{U}(P) \tag{2.41}$$

The bounding function $\mathcal{U}(P)$ can take many forms depending on the method used and the tightness of the bound desired. One bound is the Chang-Peng bound, which is defined in Eqn 2.42 [6].

$$\mathcal{U}(P) = \sum_{i=1}^{q} S_i |\Lambda_i| S_i^T \tag{2.42}$$

In this bound, S_i is defined as the orthonormal transformation that diagonalizes the symmetrical matrix $(RA_i + A_i^T R)$:

$$S_i^T (RA_i + A_i^T R) S_i = \Lambda_i \tag{2.43}$$

Then, Λ_i is a diagonal matrix of the eigenvalues of $(RA_i + A_i^T R)$, and $|\Lambda_i|$ is a diagonal matrix with elements taking absolute values of elements in Λ_i.

Another bound is the linear bound, developed in Bernstein [3]. If we define $2\alpha = \sum_{i=1}^{q} 1/\gamma_i$, then the optimization equation becomes Eqn 2.44, which is sometimes referred to as the generalized algebraic Riccati equation (GARE) [12]. We are able to choose γ_i to optimize for the desired robustness and performance.

$$0 = (A + \alpha I)^T P + P(A + \alpha I) + Q - PBR^{-1}B^T P + \sum_{i=1}^{q} \gamma_i A_i^T P A_i \tag{2.44}$$

Another bound is the quadratic bound, developed by Petersen and Hollot in [27]. In this bound, the A_i is decomposed and defined as $A_i = (\epsilon_i D_i)(1/\epsilon_i E_i)$, where ϵ_i is chosen to optimize P. This results in the optimization equation in Eqn 2.45 [12].

$$0 = A^T P + PA + Q + \sum_{i=1}^{q} \left(1/\epsilon_i^2\right) E_i^T E_i - P\left(BR^{-1}B^T - \sum_{i=1}^{q} \epsilon_i^2 D_i D_i^2\right) P \tag{2.45}$$

2.5.3 LMI Guaranteed-Cost Formulation

One way to solve the LQR problem is by solving a convex optimization problem in linear matrix inequality (LMI) form. We start with the LQR cost function in Eqn 2.46, where x is the state vector, x_0 is the initial value of the state vector, Q is a positive semidefinite matrix, R is a positive definite matrix, and K is a state-feedback gain.

$$J = \int_0^\infty x^T(Q + K^T RK)x dt \tag{2.46}$$

To solve for the state-feedback gain K, there must be a matrix P that is positive definite that satisfies Eqn 2.47.

$$\frac{d}{dt}(x^T Px) = -x^T(Q + K^T RK)x \tag{2.47}$$

Introducing the trace operator, which is the sum of all elements on the main diagonal of a square matrix, the cost function can be written as Eqn 2.48, where P satisfies Eqn 2.49

$$J = \mathrm{Tr}((Q + K^T R K)P) \tag{2.48}$$

$$(A + BK)P + P(A + BK)^T + x_0 x_0^T = 0 \tag{2.49}$$

If we define $Y = KP$ and assume that the matrix Ax_0 is controllable, the optimal feedback gain can be found by solving the optimization problem in Eqn 2.50.

$$\begin{aligned} &\min_{P,Y} \mathrm{Tr}(QP) + \mathrm{Tr}(R^{1/2} Y P^{-1} Y^T R^{1/2}) \\ \text{such that} \quad &AP + PA^T + BY + Y^T B^T + I < 0 \end{aligned} \tag{2.50}$$

To eliminate the nonlinear term $\mathrm{Tr}(R^{1/2} Y P^{-1} Y^T R^{1/2})$, another variable X is introduced. Using Schur's complement, one target of performance can be rewritten as Eqn 2.51.

$$\begin{aligned} &\min_{X} X \\ \text{such that} \quad &X > R^{1/2} Y P^{-1} Y^T R^{1/2} \longleftrightarrow \begin{bmatrix} X & R^{1/2} Y \\ Y^T R^{1/2} & P \end{bmatrix} > 0 \end{aligned} \tag{2.51}$$

Using this, the final LMI formulation of the LQR problem is shown in Eqn 2.52.

$$\begin{aligned} &\min_{P,Y,X} \mathrm{Tr}(QP) + \mathrm{Tr}(X) \\ \text{subject to} \quad & \\ &AP + PA^T + BY + Y^T B^T + I < 0 \\ &\begin{bmatrix} X & R^{1/2} Y \\ Y^T R^{1/2} & P \end{bmatrix} > 0 \\ &P > 0 \end{aligned} \tag{2.52}$$

This formulation can be extended using the polytopic uncertainty principle. If the uncertainty in the model can be explicitly bounded, then multiple LMIs can be formulated which represent the extremes, or vertices, of the region in which stability should be guaranteed. Thus, the LQR guaranteed-cost problem for a set of possible matrices $A_1, ..., A_N$ is shown in Eqn 2.53 [37].

$$\begin{aligned}
&\min_{P,Y,X} \mathrm{Tr}(QP) + \mathrm{Tr}(X) \\
\text{subject to}\quad & \\
&A_1P + PA_1^T + BY + Y^TB^T + I < 0 \\
&A_2P + PA_2^T + BY + Y^TB^T + I < 0 \\
&\quad\vdots \\
&A_NP + PA_N^T + BY + Y^TB^T + I < 0 \\
&\begin{bmatrix} X & R^{1/2}Y \\ Y^TR^{1/2} & P \end{bmatrix} > 0 \\
&P > 0
\end{aligned} \tag{2.53}$$

2.5.4 Gain Scheduling

In order to control a nonlinear system using linear methods, the system must be linearized and the controller is based on the linearized system. However, the linearization does not perfectly describe the nonlinear system and is only valid close to the point about which it was linearized. This is not a problem when the goal is to regulate to the trim point in response to small disturbances. If the goal is to track a trajectory which encompasses multiple flight regimes, the linear model and controller will not be valid throughout the entire trajectory. A solution to this is gain scheduling. Gain scheduling involves linearizing the system at multiple points along the trajectory and designing a controller for each linearization. These calculations are most often done offline and then the model and controller being used is changed based on the value of one or more scheduling variables. Gain scheduling has the advantage of being a relatively simple method where the bulk of the computational work is done offline. One problem that can arise is that at the transition points the system can be shocked by the sudden change in controller gains. This issue can be mitigated by designing a transition zone where gains are smoothly changed, or by specifying the gains as a continuous function of the scheduling variables.

Chapter 3

METHODS

This section will discuss the methodology that was used to evaluate the feasibility and performance of the rotary horizontal tail configuration. The effort to do so was according to the following steps:

1. Perform aerodynamic analysis of both the conventional and modified aircraft and compare the lift and drag profiles
2. Construct a virtual aerodynamic model of both the conventional and modified aircraft
3. Analyze and compare the static and dynamic stability of the conventional and modified aircraft
4. Design LQR feedback controllers for both linearized aircraft models and compare the performance and robustness
5. Design guaranteed-cost feedback controllers for both linearized aircraft models and compare the performance and robustness

3.1 Geometry

The geometry of the aircraft used for this analysis was based on the Cessna 172. Two geometries were used: conventional and modified. These geometries are identical, except that the vertical tail is missing in the modified geometry. Important geometric properties are shown in Table 3.1. A scale image of a Cessna 172 is shown in Figure 3.1 [1]. The moment of inertia matrix is found in Eqn 3.1, which was assumed to be equal between the conventional and modified models. While this assumption seems ill-advised, it is likely closer to the truth than expected. In reality, the mechanism to rotate the horizontal tail will likely increase the weight at the tail to what it would have been with the vertical stabilizer. While this will depend on the mechanical implementation and the individual aircraft, the simplification of assuming identical moments of inertia is reasonable for our current analysis.

Table 3.1: Aircraft geometry

Wingspan	11.0 m
MAC	1.57 m
Reference area	17.08 m^2
Wing root chord	1.69 m
Wing tip chord	1.17 m
Horizontal tail root chord	1.30 m
Horizontal tail tip chord	0.84 m
Horizontal tail span	3.48 m
Vertical tail root chord	1.49 m
Vertical tail tip chord	0.71 m
Vertical tail height	1.47 m
Main airfoil	NACA 2412
Horizontal tail airfoil	NACA 0012
Vertical tail airfoil	NACA 0009
Aileron limits	$\pm 20^o$
Elevator limits	$+23^o, -28^o$
Rudder limits	$\pm 17.7^o$

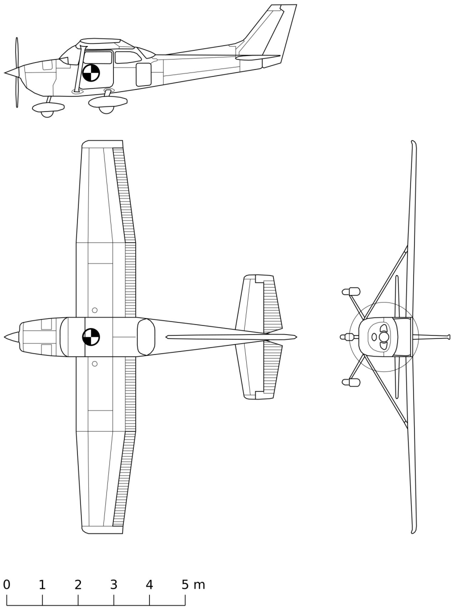

Figure 3.1: Scale drawing of Cessna 172, on which the analyzed geometry is based [1]

$$I_b = \begin{bmatrix} 197.2026 & 0 & 146.0218 \\ 0 & 1808.7634 & 0 \\ 146.0218 & 0 & 1611.5609 \end{bmatrix} kg * m^2 \tag{3.1}$$

3.2 Aerodynamic Analysis

The aerodynamic analysis was conducted using two aerodynamic software packages: xflr5 and Athena Vortex Lattice (AVL) from MIT. xflr5 is a three-dimensional solver that utilizes potential flow and empirical and theoretical turbulence models [8][10][11][9]. It first uses potential flow theory and turbulence models in XFOIL to analyze the flow over two-dimensional airfoils for multiple Reynolds numbers. From this data and potential flow theory, xflr5 solves for aerodynamic coefficients for a three-dimensional aircraft model. This software was used to determine the lift and drag profiles for the conventional and modified aircraft. However, xflr5 does not have the capability to analyze asymmetric geometries, such as when the horizontal tail is rotated about the x-axis. Therefore, to acquire the aerodynamic force and moment coefficients to be used in the control model, AVL was used. AVL is a vortex lattice method solver and thus exclusively uses potential flow theory to solve for the aerodynamic forces and moments [15]. Unlike xflr5, AVL allows for greater variation and asymmetry in aircraft geometry.

Other open-source software packages were considered, but ultimately decided against in favor of AVL and xflr5. The most trust was placed in the results from xflr5 because of its incorporation of empirical data and increased complexity, and so candidate programs were compared against its results. One program considered was Open Vehicle Sketch Pad (OpenVSP) with VSPAERO. VSPAERO is a 3-dimensional potential flow aerodynamics tool for detailed conceptual aircraft analysis [22]. While this is a promising tool, the process to learn to properly model the conventional and modified aircraft was deemed too complex for the time constraints of this effort. Another considered program was Tornado, which also uses a 3D-vortex lattice method with a flexible wake and runs through MATLAB [23]. Tornado was easy to use, conveniently in MATLAB, and could handle tail rotation. However, when compared to xflr5 and AVL, it consistently calculated aerodynamic coefficients significantly greater in magnitude than both xflr5 and AVL. Because of this, Tornado was judged to be less accurate than AVL, which was closer to the xflr5 results.

Aerodynamic coefficients and derivatives were calculated for an airspeed of 68 m/s, at standard atmosphere sea level conditions, and for angles of attack and sideslip between 14 and -14 degrees in increments of 2 degrees. Aerodynamic control derivatives were also calculated at 0 degrees angle of attack and sideslip for full deflections of each control surface. For the modified model, all these test points were repeated for tail rotation angles ranging from 0 to 90 degrees by increments of 15 degrees. All test points for both configurations were for a Reynolds number of 8.7317×10^6.

3.3 Aerodynamic Model

The aerodynamic model was developed in MATLAB and simulated using MATLAB Simulink. It is a nonlinear model with 12 states and 4 control inputs [34]. The state and control vectors are given in Eqn 3.2. Using curve fits and derivatives from the aerodynamic analysis, the force and moment coefficients are calculated at the given state and control input. From these coefficients, the new state is calculated.

$$\begin{aligned} \vec{x} &= \begin{bmatrix} u & v & w & p & q & r & \phi & \theta & \psi & P_N & P_E & P_D \end{bmatrix}^T \\ \vec{u}_{conventional} &= \begin{bmatrix} \delta_a & \delta_e & \delta_r & \delta_t \end{bmatrix}^T \\ \vec{u}_{modified} &= \begin{bmatrix} \delta_a & \delta_e & \delta_{tail} & \delta_t \end{bmatrix}^T \end{aligned} \tag{3.2}$$

Two rigid-body models were created in MATLAB, one for the conventional aircraft and one for the modified aircraft. The models use the following steps: Define constants and intermediate variables, calculate aerodynamic coefficients in the stability axis, calculate aerodynamic forces in the body axis, calculate moment coefficients and moments in the body axis about the center of gravity, add propulsion and gravity effects, and calculate the new states.

The lift coefficient is calculated using an equation derived from xflr5 data for the whole aircraft. For both the conventional and modified model, a cubic curve fit with reliance only on the angle of attack was used. Any lift coefficient dependence on sideslip angle or tail rotation angle was assumed to be negligible, and this assumption was shown by the xflr5 and AVL simulations to be reasonable. Similarly, the drag coefficient curve fit was determined from xflr5 data assuming quadratic dependence on angle of attack only. While the sideslip angle and control deflection do typically have a significant effect on drag coefficient, for this study these effects are small enough to ignore. The function for side force coefficient was more complicated to determine. For the conventional aircraft, side force coefficient depends primarily on sideslip angle and rudder deflection. Both the sideslip and rudder deflection contributions are calculated using a linear curve fit from xflr5 and AVL data, respectively. The combination of these effects was assumed to be linear and so they are summed. For the modified aircraft, the function for side force coefficient was determined using only AVL data. Similar to the conventional, side force coefficient is assumed to be a linear combination of the effect due to sideslip angle and elevator deflection. However, the contribution of each depends on the tail rotation angle and is assumed to be a sinusoidal relationship. The curve fit equations used for the conventional model are shown in Eqns 3.4, 3.5, and 3.6 and the equations for the modified model are shown in Eqns 3.8, 3.9, and 3.10.

$$\textbf{Conventional} \tag{3.3}$$

$$C_L = -1.979\alpha^3 - 0.1339\alpha^2 + 5.1882\alpha + 0.1514 \tag{3.4}$$

$$C_D = 1.1827\alpha^2 + 0.0582\alpha + 0.0089 \tag{3.5}$$

$$C_Y = -0.17299\beta + 0.1293\delta_r \tag{3.6}$$

$$\textbf{Modified} \tag{3.7}$$

$$C_L = -1.9779\alpha^3 - 0.1339\alpha^2 + 5.1846\alpha + 0.1512 \tag{3.8}$$

$$C_D = 1.1821\alpha^2 + 0.0581\alpha + 0.0085 \tag{3.9}$$

$$C_Y = (0.3578\cos(2\delta_{tail}) - 0.3578)\beta + 0.0096\delta_e\sin(\delta_{tail}) \tag{3.10}$$

The aerodynamic coefficients are then used to calculate the forces in the body axis, according to Eqn 3.11. The forces are then rotated from the stability axis to the body axis according to Eqn 3.12.

$$F_{A_s} = \begin{bmatrix} -C_D q S \\ C_Y q S \\ -C_L q S \end{bmatrix} \tag{3.11}$$

$$F_{A_b} = \begin{bmatrix} \cos\alpha & 0 & -\sin\alpha \\ 0 & 1 & 0 \\ \sin\alpha & 0 & \cos\alpha \end{bmatrix} F_{A_s} \tag{3.12}$$

For both models, the aerodynamic moments are calculated by summing the contributions of the static stability, dynamics, and controls, according to Eqn 3.13. For the conventional model, this process is fairly straightforward. The contribution of static stability was curve fit to xflr5 data, such that rolling moment coefficient is a cubic function of sideslip angle, pitching moment coefficient is a cubic function of angle of attack, and yawing moment coefficient is a linear function of sideslip angle, according to Eqn 3.14. The dynamics contribution is a matrix of derivatives whose values were found using xflr5 and are shown in Eqn 3.15. The control derivatives, shown in Eqn 3.16, were similarly found using AVL. The moments are then calculated from the coefficients according to Eqn 3.17 and then rotated into the body axis from the stability axis according to Eqn 3.18

$$C_{M_{cg_s}} = \bar{\eta} + \frac{dC_M}{d\omega}\omega_{bc} + \frac{dC_M}{du}u \tag{3.13}$$

$$\bar{\eta} = \begin{bmatrix} -0.1422\beta^3 - 0.0112\beta \\ 1.3246\alpha^3 - 1.9218\alpha^2 - 2.069\alpha - 0.0461 \\ 0.1193\beta \end{bmatrix} \tag{3.14}$$

$$\frac{dC_M}{d\omega} = \begin{bmatrix} -0.54597 & 0 & 0.031232 \\ 0 & -14.841 & 0 \\ -0.006825 & 0 & -0.11954 \end{bmatrix} \frac{\bar{c}}{V_A} \tag{3.15}$$

$$\frac{dC_M}{du} = \begin{bmatrix} 0.009614 & 0 & 0.000183 \\ 0 & -0.029862 & 0 \\ -0.000401 & 0 & -0.001080 \end{bmatrix} \frac{180}{\pi} \tag{3.16}$$

$$M_{A_{cg_s}} = \begin{bmatrix} C_l q b_{ref} S \\ C_m q \bar{c} S \\ C_n q b_{ref} S \end{bmatrix} \tag{3.17}$$

$$M_{A_{cg_b}} = \begin{bmatrix} \cos\alpha & 0 & -\sin\alpha \\ 0 & 1 & 0 \\ \sin\alpha & 0 & \cos\alpha \end{bmatrix} M_{A_{cg_s}} \tag{3.18}$$

This process is complicated for the modified aircraft because the tail rotation angle significantly impacts the static stability, dynamic derivatives, and control derivatives. It was assumed that the tail rotation angle affected the moment contributions according to a sinusoidal function. Equations 3.19 through 3.21 show the values and equations produced by curve-fitting AVL data. Various assumptions and simplifications were made which are reflected in these equations.

$$\bar{\eta} = \begin{bmatrix} (0.0102\cos(2\delta_{tail}) - 0.0148)\beta \\ (-0.6548\cos(2\delta_{tail}) - 1.3045)\alpha - 0.0787 \\ (-0.15115\cos(2\delta_{tail}) + 0.15115)\beta - 0.0987\alpha\sin(2\delta_{tail}) \end{bmatrix} \tag{3.19}$$

$$\frac{dC_M}{d\omega} = \begin{bmatrix} -0.481 & 0.065\sin(2\delta_{tail}) & 0.010\sin(2\delta_{tail}-\pi/2)+0.052 \\ 0.124\sin(2\delta_{tail}) & 6.728\sin(2\delta_{tail}-\pi/2)-8.251 & -1.048\sin(2\delta_{tail}) \\ 0.015\sin(2\delta_{tail}-\pi/2)+0.004 & -0.968\sin(2\delta_{tail}) & -0.149\sin(2\delta_{tail}-\pi/2)-0.150 \end{bmatrix} \frac{\bar{c}}{V_A} \tag{3.20}$$

$$\frac{dC_M}{du} = \begin{bmatrix} 0.009614 & 0.000262\sin(\delta_{tail}) \\ 0 & -0.0299\cos(\delta_{tail}) \\ -0.000401 & -0.00427\sin(\delta_{tail}) \end{bmatrix} \frac{180}{\pi} \tag{3.21}$$

$$\tag{3.22}$$

The propulsion effects in the body axis are calculated by the equations shown in Eqn 3.23 and 3.24. These equations assume that the single engine is perfectly aligned in the body frame x-axis and that the maximum thrust of the engine is 25% of the weight of the aircraft.

$$F_{E_b} = \begin{bmatrix} 0.25mg\delta_t \\ 0 \\ 0 \end{bmatrix} \tag{3.23}$$

$$M_{E_b} = \begin{bmatrix} X_{cg} - X_{apt} \\ Y_{cg} - Y_{apt} \\ Z_{cg} - Z_{apt} \end{bmatrix} \times F_{E_b} \tag{3.24}$$

The calculation of gravity effects is shown in Eqn 3.25.

$$F_{g_b} = \begin{bmatrix} -g\sin(\theta) \\ g\cos(\theta)\sin(\phi) \\ g\cos(\theta)\cos(\phi) \end{bmatrix} * m \tag{3.25}$$

Finally, the new states are calculated. The aerodynamic, propulsion, and gravitational forces and moments are summed in the body axis, where the total force in the body axis is

F_b and the total moment in the body axis about the CG is M_{cg_b}. These are used in Eqns 3.26 through 3.29 to calculate the new states, where the new states are on the left hand side and the old states are input to the right hand side.

$$\begin{bmatrix} u \\ v \\ w \end{bmatrix} = \frac{1}{m} F_b - \omega_{bc} \times V_b \tag{3.26}$$

$$\begin{bmatrix} p \\ q \\ r \end{bmatrix} = I_b^{-1} (M_{cg_b} - \omega_{bc} \times (I_b \omega_{bc})) \tag{3.27}$$

$$\begin{bmatrix} \phi \\ \theta \\ \psi \end{bmatrix} = \begin{bmatrix} 1 & \sin(\phi)\tan(\theta) & \cos(\phi)\tan(\theta) \\ 0 & \cos(\phi) & -\sin(\phi) \\ 0 & \sin(\phi)/\cos(\theta) & \cos(\phi)/\cos(\theta) \end{bmatrix} \omega_{bc} \tag{3.28}$$

$$\begin{bmatrix} P_N \\ P_E \\ P_D \end{bmatrix} = \begin{bmatrix} \cos\theta\cos\psi & \cos\theta\sin\psi & -\sin\theta \\ -\cos\phi\sin\psi + \sin\phi\sin\theta\cos\psi & \cos\phi\cos\psi + \sin\phi\sin\theta\sin\psi & \sin\phi\cos\theta \\ \sin\phi\sin\psi + \cos\phi\sin\theta\cos\psi & -\sin\phi\cos\psi + \cos\phi\sin\theta\sin\psi & \cos\phi\cos\theta \end{bmatrix}^T V_b \tag{3.29}$$

3.3.1 Data Curve Fits

The equations used in the aerodynamic model are derived directly from curve fits of the data. For the conventional model, this process was fairly simple and standard, as valid simplifications can be made such that each coefficient depends on only one variable or a linear combination of two variables. These assumptions break down for the modified model since there are nonlinear dependencies on the tail rotation angle for most coefficients.

Figure 3.2 shows the AVL-calculated lift coefficient versus angle of attack at various tail rotation angles. While there is some change in lift coefficient at high angles of attack, this change is at most 7.64%. While this is an aerodynamically significant change, for the purposes of demonstrating controllability this difference is negligible. Therefore, the lift coefficient in the model does not depend on tail rotation angle. This extends also to drag coefficient intuitively, since drag can be decomposed into primarily skin friction and induced drag. Since tail rotation angle does not affect significantly either the wetted area or the lift coefficient, drag coefficient does not significantly depend on tail rotation angle.

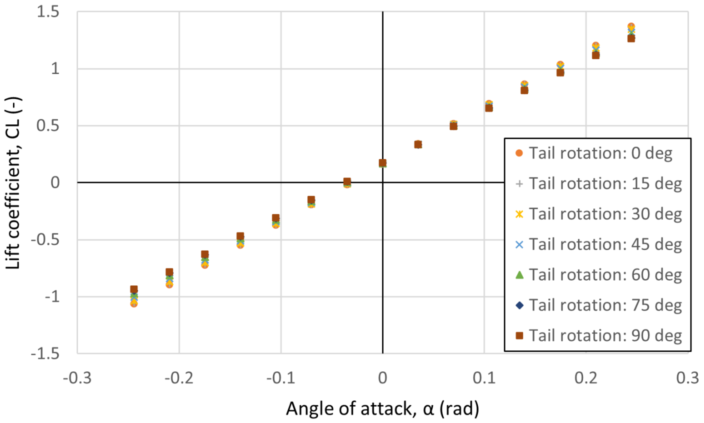

Figure 3.2: Lift coefficient data from AVL for the modified aircraft at various tail rotation angles

Figure 3.4a shows that the side force coefficient changes significantly with the tail rotation angle. Because the tail is not cambered and not at a dihedral and fuselage effects are ignored, the slope for zero tail rotation angle is zero and the intercept for all rotation angles is $(0, 0)$. The only factor that changes is the slope of the curve, or C_{Y_β}. Based on Figure 3.4b, the relationship between C_{Y_β} and tail rotation angle was determined to be sinusoidal, described by Eqn 3.10. The contribution to side force by the elevator control deflection was assumed to be linearly related to deflection angle and sinusoidally dependent on tail rotation angle, based on Figure 3.4.

Figure 3.5 shows the relationship between C_{l_β} and tail rotation angle. This derivative increases as the tail rotation angle approaches 90 degrees since the tail is affected more by the sideslip when aligned vertically.

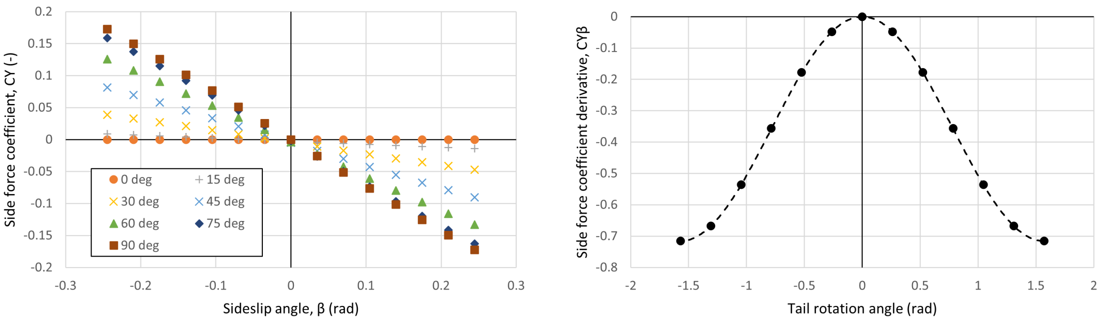

(a) Side force coefficient at various tail rotation angles

(b) Side force derivative with respect to sideslip angle

Figure 3.3: Relationship between side force coefficient and tail rotation angle for the modified aircraft

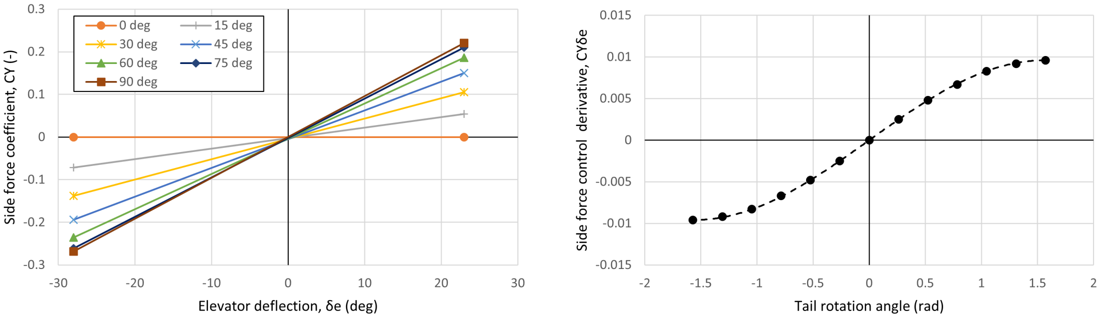

(a) Side force coefficient at various tail rotation angles

(b) Side force derivative with respect to elevator deflection

Figure 3.4: Relationship between elevator side force control power and tail rotation angle for the modified aircraft

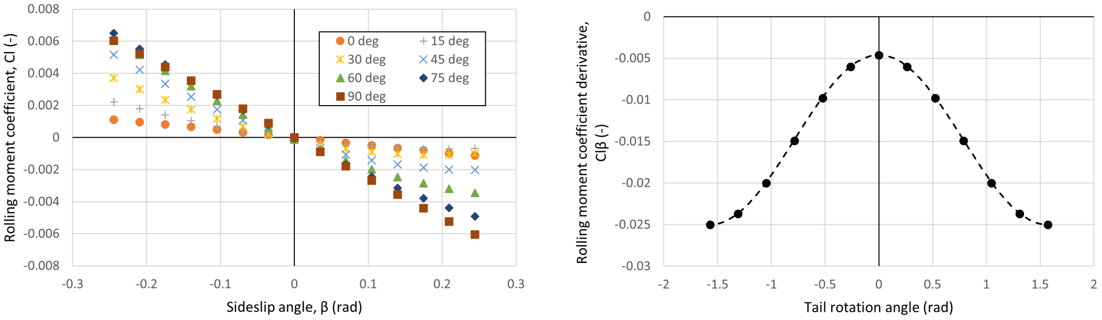

(a) Rolling moment coefficient at various tail rotation angles

(b) Rolling moment derivative with respect to sideslip angle

Figure 3.5: Relationship between rolling moment coefficient and tail rotation angle for the modified aircraft

Figure 3.6 shows the relationship between C_{m_α} and tail rotation angle. This shows a similar but opposite relationship as C_{l_β}, since the tail provides the most longitudinal stability when horizontally aligned.

The relationship between C_{n_β} and tail rotation angle is presented in Figure 3.7. This shows a similar relationship to Figure 3.5, since a vertically aligned tail providies the greatest directional impact.

On a conventional aircraft, there is no significant relationship between angle of attack and yawing moment coefficient, especially at zero sideslip angle. However, with the tail rotated, the tail produces lift when at an angle of attack that is both in the y- and z- axes. This lift force component in the y-axis causes a yawing moment. Therefore, the yawing moment coefficient depends on angle of attack as well, which is shown in Figure 3.8. Unlike the relationship to C_{n_β}, C_{n_α} is zero when the tail is either horizontal or vertical and is positive or negative depending on the direction of rotation.

Figures 3.9, 3.10, and 3.11 show the relationships between tail rotation angle and the dynamic derivatives. All these derivatives are sinusoidally related to tail rotation angle

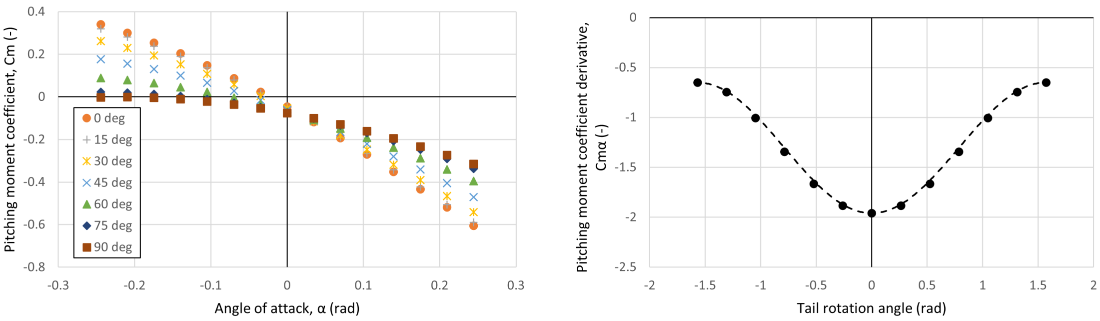

(a) Pitching moment coefficient at various tail rotation angles

(b) Pitching moment derivative with respect to angle of attack

Figure 3.6: Relationship between pitching moment coefficient and tail rotation angle for the modified aircraft

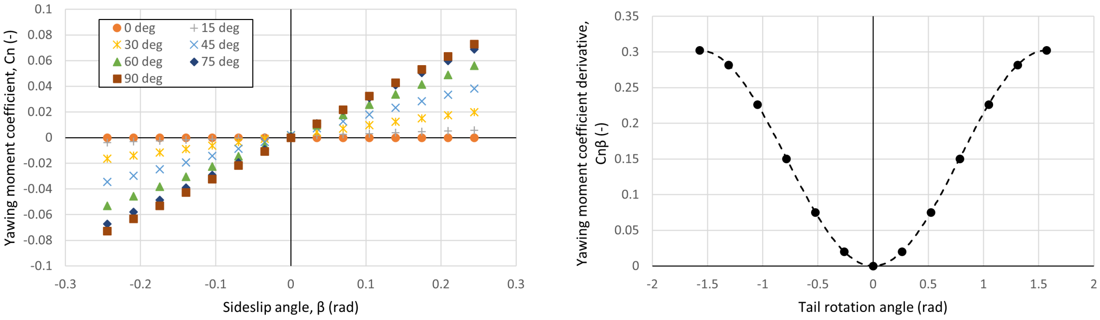

(a) Yawing moment coefficient at various tail rotation angles

(b) Yawing moment derivative with respect to sideslip angle

Figure 3.7: Relationship between yawing moment coefficient, tail rotation angle, and sideslip angle for the modified aircraft

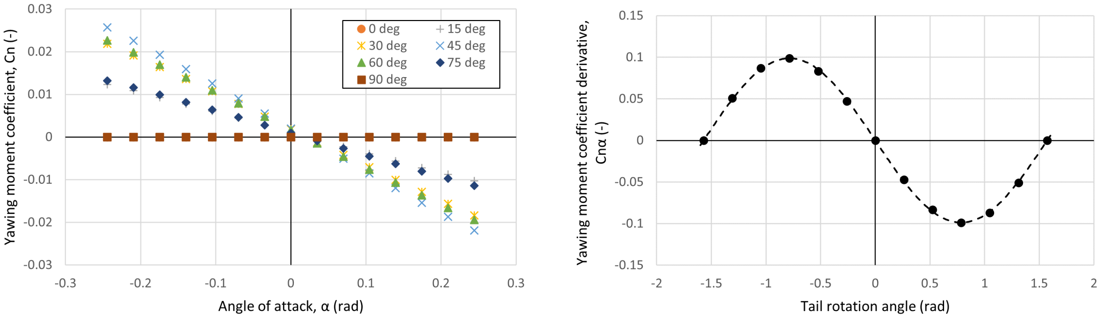

(a) Yawing moment coefficient at various tail rotation angles

(b) Yawing moment derivative with respect to angle of attack

Figure 3.8: Relationship between yawing moment coefficient, tail rotation angle, and angle of attack for the modified aircraft

except for the roll damping derivative in Figure 3.9a. C_{l_p} is nearly constant because the amount of surface area resisting a roll rate is constant regardless of tail rotation angle. The dashed lines show the analytical curve fits, which match very well with most of the data. Only Figures 3.10a and 3.11a show significant deviations from the prediction.

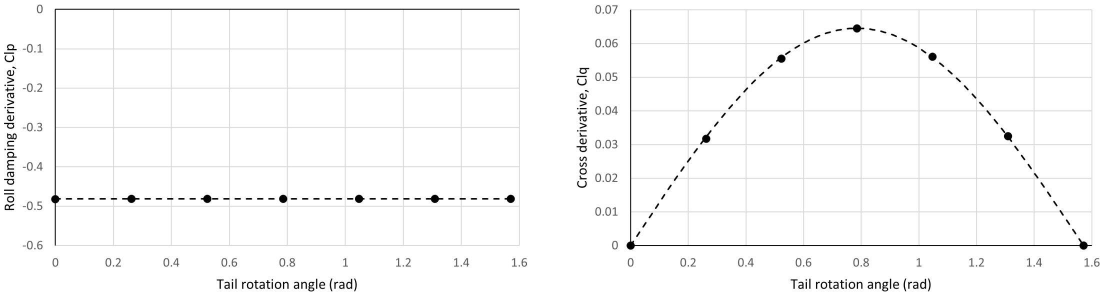

(a) Roll damping derivative

(b) Pitch rate cross derivative

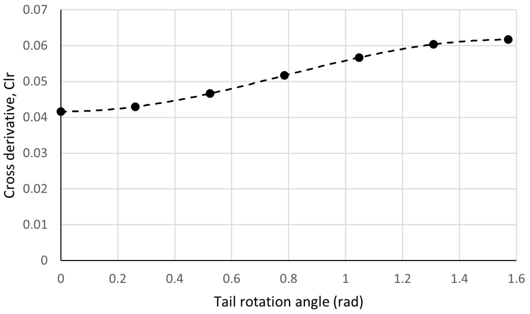

(c) Yaw rate cross derivative

Figure 3.9: Curve fits of rolling moment dynamic derivatives over various tail rotation angles

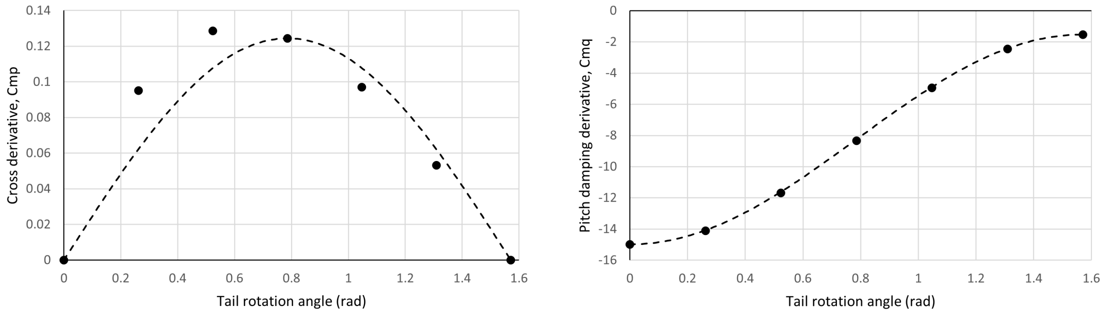

(a) Roll rate cross derivative

(b) Pitch damping derivative

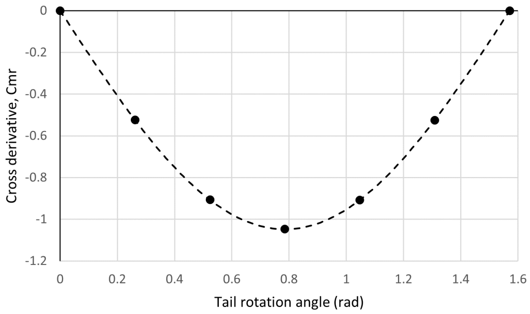

(c) Yaw rate cross derivative

Figure 3.10: Curve fits of pitching moment dynamic derivatives over various tail rotation angles

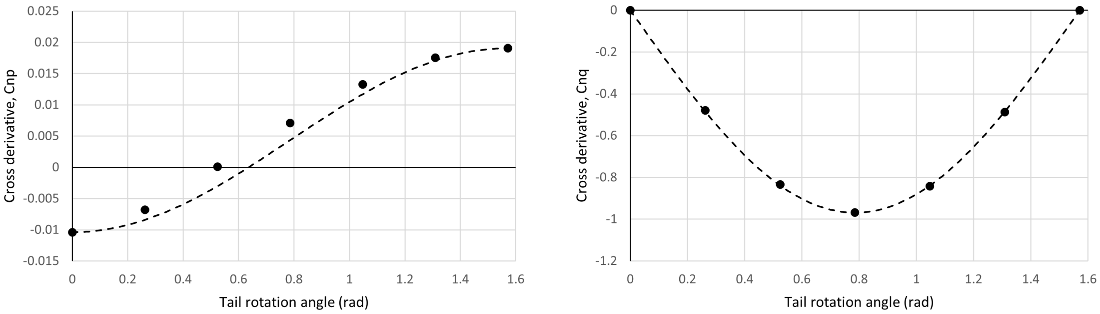

(a) Roll rate cross derivative

(b) Pitch rate cross derivative

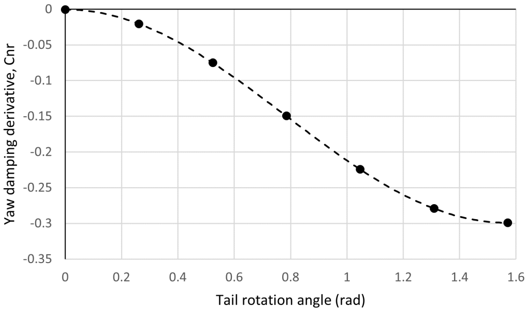

(c) Yaw damping derivative

Figure 3.11: Curve fits of yawing moment dynamic derivatives over various tail rotation angles

3.4 Stability Analysis

The nonlinear models are implicitly linearized about the straight and level trim condition and their stability characteristics analyzed. Firstly, the static stability derivatives were calculated for both the conventional and modified aircraft. These derivatives are determined from the aerodynamic data and include C_{l_β}, C_{m_α}, and C_{n_β}. Next, the dynamic stability modes were compared. These modes include the short period, phugoid, Dutch roll, roll subsidence, and spiral modes, and are characterized by the eigenvalues of the linearized state-space equations. They are also characterized by the time constant, natural frequency, and damping ratio, which were compared to determine the effect of the modification. The eigenvalues were matched to the corresponding mode based on the associated eigenvectors, which showed the states the pole most affected.

3.5 Controller Design

3.5.1 Linear Quadratic Regulator

To control both models, LQR was used to find the optimal state-feedback gain. In Simulink, this was incorporated as a feedback loop which multiplies the feedback gain matrix K by the state x, which produces the control input u. The control input is limited in both rate and maximum deflections, shown in Table 3.2, based on the limits presented by the BIRE paper [20].

To calculate the LQR optimal gain matrix, the models were first linearized about a trim point. Then state and control penalty matrices, Q and R, were determined. Bryson's rule was followed to determine initial values and then tuned for desired response characteristics. The linear model and penalty matrices were used with the MATLAB command **lqr()** to calculated the controller matrix K. In order to properly compare the conventional and modified models, the penalty matrices were the same for both controllers.

Table 3.2: Control rate and deflection limits

Aileron deflection limit	$\pm 20^o$
Elevator deflection limit	$+23^o, -28^o$
Rudder deflection limit	$\pm 17.7^o$
Tail rotation deflection limit	$\pm 90^o$
Aileron rate limit	$80\ deg/s$
Elevator rate limit	$60\ deg/s$
Rudder rate limit	$120\ deg/s$
Tail rotation rate limit	$120\ deg/s$

3.5.2 Polytopic Uncertainty Guaranteed-Cost Design

To implement the LMI formulation of the LQR problem with polytopic uncertainty, CVX in MATLAB with the MOSEK solver was used to solve the optimization problem in Eqn 3.30 [37].

$$\begin{aligned} &\min_{P,Y,X} \operatorname{Tr}(QP) + \operatorname{Tr}(X) \\ \text{subject to} \quad & \\ &A_1 P + P A_1^T + BY + Y^T B^T + I < 0 \\ &A_2 P + P A_2^T + BY + Y^T B^T + I < 0 \\ &\ \vdots \\ &A_N P + P A_N^T + BY + Y^T B^T + I < 0 \\ &\begin{bmatrix} X & R^{1/2} Y \\ Y^T R^{1/2} & P \end{bmatrix} > 0 \\ &P > 0 \end{aligned} \tag{3.30}$$

First, the A and B matrices from the dynamics and the penalty matrices Q and R are defined. Then the maximum percent uncertainty is defined for all the uncertain positions. Only uncertainties in positions (2,2), (2,4), (4,2), (4,4), (4,6), (6,2), (6,4), and (6,6) in the A-matrix and (2,3), (4,3), and (6,3) in the B-matrix were designed for. These positions correspond to interactions between the states v (side velocity), p (roll rate), and r (yaw rate) and were chosen because intuitively, and in actuality, these values showed the most difference between the conventional and modified systems. Furthermore, these positions will likely be the most uncertain when conducting system identification for the modified aircraft because the rotary tail leads to complex coupling between the lateral-directional moments and forces, as seen in previous sections. The number of perturbed positions had to be limited to reduce the number of LMIs that must be solved. Using the MATLAB function **combvec**, all possible combinations of the maximum applied uncertainty in each position of the A- and B-matrix could be accounted for. These combinations are then used to create N number of LMIs, where $N = 2^{(\text{\# of perturbed positions})}$. The result of the optimization is a solution for P and Y, which are then used to calculate the state-feedback gain $K = -YP^{-1}$.

3.6 Performance and Robustness Analysis

The performance of the controlled models was analyzed using multiple metrics. The poles of the system, or the eigenvalues of the matrix given by $A + BK$, were compared to show dynamic stability characteristics. Also, the time domain step performance metrics of steady state offset, rise time, settling time, overshoot, and decay ratio were used. Definitions of these metrics are found in Skogestad's book [31].

The robustness of the systems were analyzed through the singular values of the closed-loop transfer function and the sensitivity functions, and through direct stochastic perturbation. The maximum and minimum singular values of the loop transfer function were calculated over a range of frequencies and compared between the conventional and modified systems. The same was done for the maximum singular values of the input and output sensitivity and cosensitivity functions. For the stochastic perturbation analysis, the A- and B-matrices of the systems were directly perturbed and the stability of the system was evaluated by looking at the eigenvalues. Only positions (2,2), (2,4), (4,2), (4,4), (4,6), (6,2), (6,4), and (6,6) in the A-matrix and (2,3), (4,3), and (6,3) in the B-matrix were perturbed. The perturbations applied were random Gaussian addition to the chosen positions of a percentage of the actual model value. At each maximum percentage, 1,000,000 iterations of random perturbations were done and the maximum percentage was reduced until none of the iterations resulted in an unstable system.

Chapter 4

RESULTS AND DISCUSSION

4.1 Aerodynamic Analysis

The following figures contain the results of the xflr5 simulations for an aircraft similar to the Cessna 172. Figure 4.1 shows that the removal of the vertical tail has very little effect on the lift curve. Figure 4.2 shows that removing the vertical tail results in a maximum drag reduction of approximately 6%. The reduction in drag approaches zero as the angle of attack increases, likely because the wake of the wing and horizontal tail decreases the effectiveness of the vertical tail on the conventional aircraft. Figure 4.3 shows that this drag reduction leads to a maximum increase in the lift-to-drag ratio magnitude of approximately 6%. This increase would lead to greater range and better efficiency.

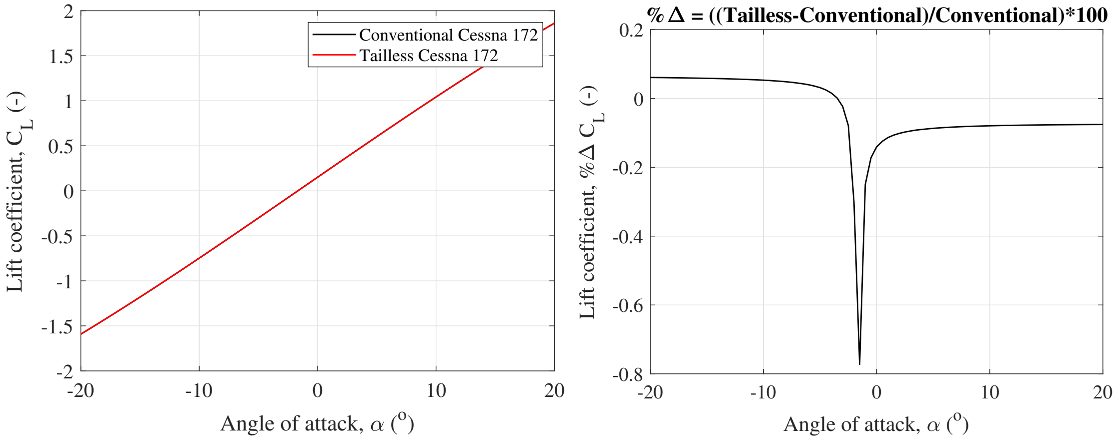

(a) Lift coefficient for both configurations (b) Percent difference in lift coefficient

Figure 4.1: Comparison of the lift coefficient for the conventional and modified aircraft similar to the Cessna 172

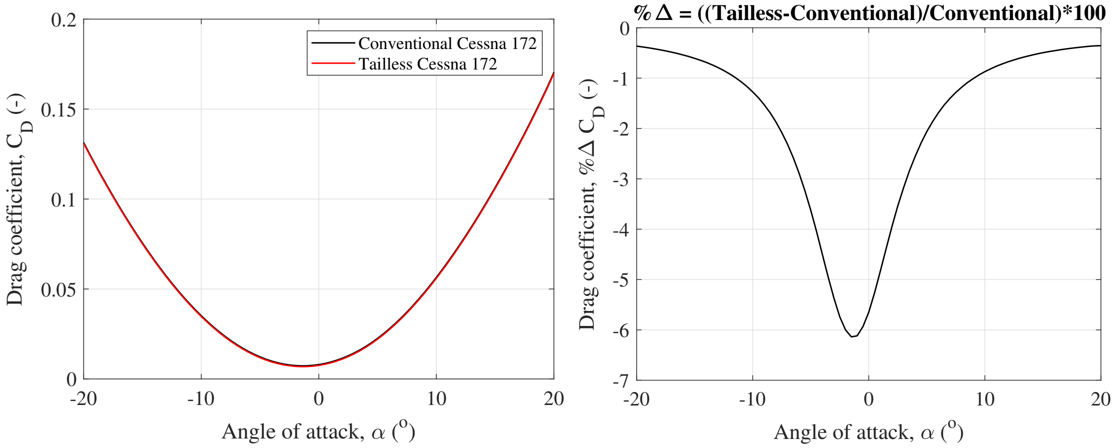

(a) Drag coefficient for both configurations (b) Percent difference in drag coefficient

Figure 4.2: Comparison of the drag coefficient for the conventional and modified aircraft similar to the Cessna 172

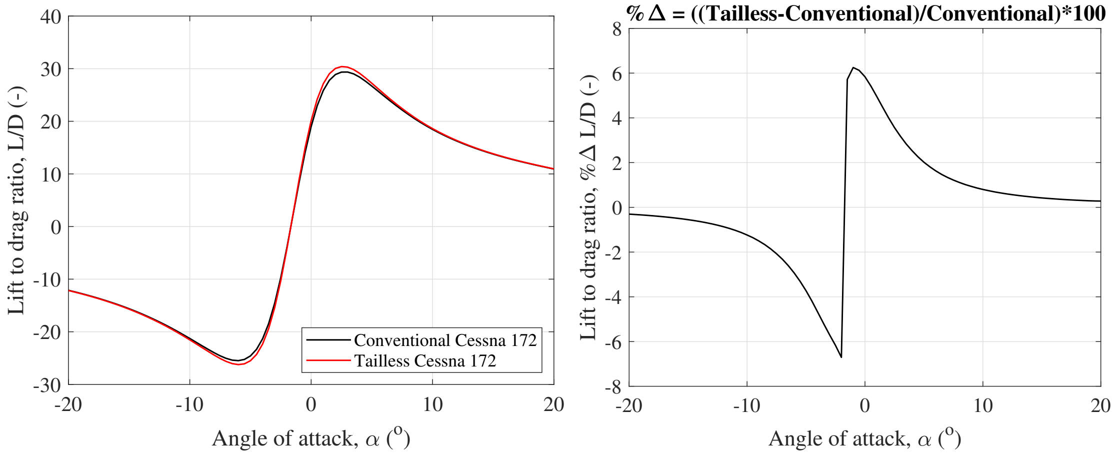

(a) Lift-to-drag ratio for both configurations (b) Percent difference in lift-to-drag ratio

Figure 4.3: Comparison of the lift-to-drag ratio for the conventional and modified aircraft similar to the Cessna 172

4.2 Stability Analysis

4.2.1 Static Stability

Figure 4.4 shows the moment coefficient results from AVL for the conventional and modified aircraft with zero tail rotation. Figure 4.4a shows the roll static stability of both the conventional ans modified model. The derivative (C_{l_β}) increases by 58.9% from the conventional to the modified, which indicates a decrease in the static roll stability. This is expected, as the vertical tail provides some roll stability on a conventional aircraft. The longitudinal static stability derivative (C_{m_α}), shown in Figure 4.4b, increases by 5.30% from the conventional to the modified model. Since a negative C_{m_α} is desirable, this indicates a slight decrease in longitudinal stability. This change is surprising, as the vertical tail should have a minimal effect on the longitudinal stability in straight and level flight, but could be caused by complicated interference flow around the junction of the horizontal and vertical tails. In Figure 4.4c, the change in directional static stability is shown, characterized by the derivative C_{n_β}. The derivative becomes zero for the modified aircraft, indicating neutral static stability, which is expected because the vertical tail provides most of the directional stability for a conventional aircraft. However, in reality a tailless aircraft would likely retain some directional stability due to the fuselage providing some vertical surface for a ”weathercock” effect.

While these results likely reflect the true trends for a physical aircraft, since AVL uses an inviscid solver there may be viscous or interference effects that affect the static stability in unforeseen ways.

4.2.2 Dynamic Stability

In steady level flight, the eigenvalues of the linearized system characterize the dynamic modes of the aircraft. Table 4.1 shows the poles and associated characteristics of the uncontrolled conventional model, while Table 4.2 shows the same information for the modified model.

The modification increased the short period damping ratio by 2.01%, while decreasing the natural frequency by 1.30%. Furthermore, the modification decreased both the damping

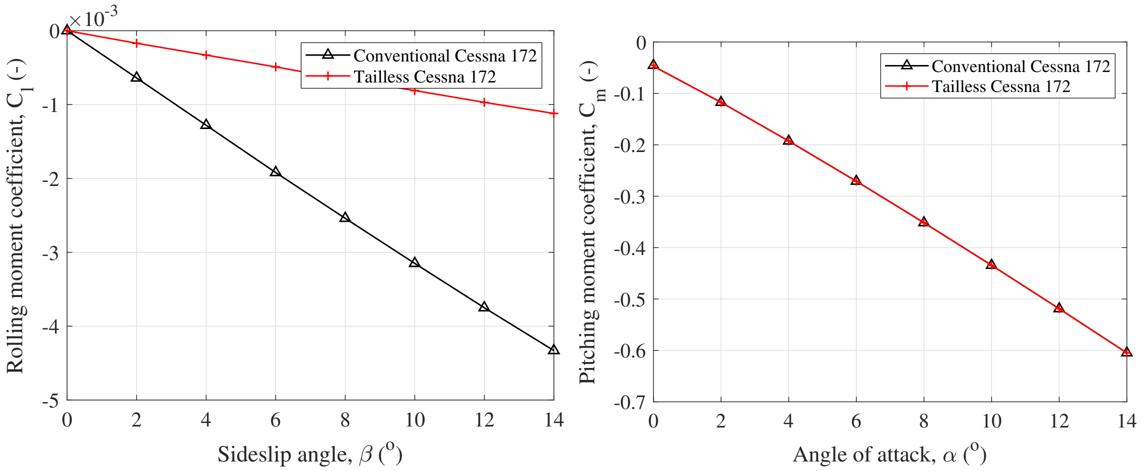

(a) Rolling moment coefficient

(b) Pitching moment coefficient

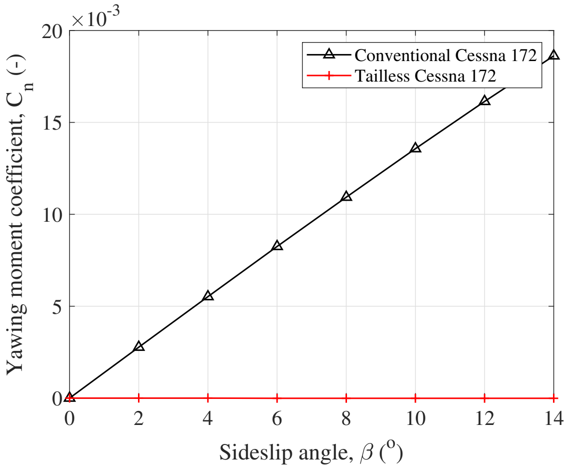

(c) Yawing moment coefficient

Figure 4.4: Comparison of the moment coefficients for the conventional and modified aircraft similar to the Cessna 172

ratio and natural frequency of the phugoid by 2.39% and 1.39%, respectively. Previous work has differed on the effect of the removal of the vertical tail on the longitudinal dynamic modes [20][35]. However, the removal of the vertical tail likely has little aerodynamic effect on the longitudinal stability of the aircraft, assuming the conventional aircraft has a vertical tail that is purely in the x-z plane. Any real effect on the longitudinal stability will likely be due to complex interference flow effects that are not able to be captured accurately by VLM flow solvers. Ultimately, these changes result in differences in the short period and phugoid periods of at most hundredths of seconds, which is inconsequential in practice.

The Dutch roll mode is greatly affected by the modification, with a reduction in damping ratio of 28.04% and a reduction in natural frequency of 95.27%. While the Dutch roll is still stable, it is barely so, with characteristics similar to the phugoid mode. Because the modified aircraft's roll stability is much greater than its yaw stability, this would likely translate to very large and slow yaw oscillations with little deviation in the roll angle. Previous research found that the Dutch roll mode became non-traditional with the loss of the vertical tail, where the poles were a set of a positive and negative real number [20][35]. Because this paper and the cited efforts utilized basic aerodynamic software and modeling, it cannot be concluded whether the Dutch roll becomes unstable. However, it is clear that the loss of the vertical tail severely degrades the Dutch roll characteristics to the point that a stabilizing control system is necessary.

The roll mode time constant increased by 13.09%, which corresponds to the roll damping. This increase is expected, since the vertical tail provides some roll damping.

The spiral mode goes from slightly unstable in the conventional model to slightly stable for the modified model. Spiral stability can be predicted by the ratio of the lateral to directional stability (C_{l_β}/C_{n_β}), where a larger ratio is associated with a stable spiral mode [38]. Because the modified model lost all directional stability, this ratio approaches infinite magnitude and the spiral mode becomes stable.

Due to the model having states for the north, east, and down positions, there are four eigenvalues corresponding to the modes affecting the position. In the uncontrolled model, these poles are zero.

Table 4.1: Uncontrolled conventional aircraft dynamic mode characteristics

Dynamic Mode	**Pole**	**Damped frequency** ω_D (rad/s)	**Natural frequency** ω_N (rad/s)	**Damping ratio** ζ (-)	**Time constant** $\tau(s)$	**Time to double** T_2 (s)
Short period	$-10.277 \pm 8.100i$	8.099	13.0815	0.7853	-	-
Phugoid	$-0.008 \pm 0.151i$	0.1506	0.1508	0.0544	-	-
Dutch Roll	$-0.644 \pm 6.441i$	6.4412	6.4734	0.0995	-	-
Roll	-36.311	-	-	-	0.0275	-
Spiral	0.005	-	-	-	-	130.78
Longitudinal	0	-	-	-	-	-
Longitudinal	0	-	-	-	-	-
Lateral	0	-	-	-	-	-
Lateral	0	-	-	-	-	-

Table 4.2: Uncontrolled modified aircraft dynamic mode characteristics

Dynamic Mode	**Pole**	**Damped frequency** ω_D (rad/s)	**Natural frequency** ω_N (rad/s)	**Damping ratio** ζ (-)	**Time constant** $\tau(s)$	**Time to double** T_2 (s)
Short period	$-10.343 \pm 7.729i$	7.7288	12.9119	0.8011	-	-
Phugoid	$-0.008 \pm 0.149i$	0.1485	0.1487	0.0531	-	-
Dutch Roll	$-0.022 \pm 0.305i$	0.3052	0.3060	0.0716	-	-
Roll	-32.108	-	-	-	0.0311	-
Spiral	-0.002	-	-	-	434.78	-
Longitudinal	0	-	-	-	-	-
Longitudinal	0	-	-	-	-	-
Lateral	0	-	-	-	-	-
Lateral	0	-	-	-	-	-

4.3 LQR Control

The models were trimmed at the straight, level, unaccelerated flight (SLUF) condition, for which the trim state and control vectors are shown in Eqn 4.1.

$$x^*_{conv} = \begin{bmatrix} 68.0000 \\ 0.0000 \\ 0.0197 \\ 0.0000 \\ 0.0000 \\ 0.0000 \\ 0.0000 \\ 0.0003 \\ 0.0000 \\ 0.0000 \\ 0.0000 \\ 0.0000 \end{bmatrix}, u^*_{conv} = \begin{bmatrix} 0.0000 \\ -0.0270 \\ 0.0000 \\ 0.2333 \end{bmatrix}, x^*_{mod} = \begin{bmatrix} 68.0000 \\ 0.0000 \\ 0.0224 \\ 0.0000 \\ 0.0000 \\ 0.0000 \\ 0.0000 \\ 0.0003 \\ 0.0000 \\ 0.0000 \\ 0.0000 \\ 0.0000 \end{bmatrix}, u^*_{mod} = \begin{bmatrix} 0.0000 \\ -0.0460 \\ 0.0000 \\ 0.2229 \end{bmatrix} \tag{4.1}$$

The penalty matrices used for both the conventional and modified linear models are shown in Eqn 4.2. Only the position states, P_N, P_E, P_D, are weighted since the position is the only state of importance when tracking a trajectory. The R matrix values are multiplied by a factor of 55 to restrain the commanded control inputs within the limitations imposed externally.

$$Q = \begin{bmatrix} 0&0&0&0&0&0&0&0&0&0&0&0\\ 0&0&0&0&0&0&0&0&0&0&0&0\\ 0&0&0&0&0&0&0&0&0&0&0&0\\ 0&0&0&0&0&0&0&0&0&0&0&0\\ 0&0&0&0&0&0&0&0&0&0&0&0\\ 0&0&0&0&0&0&0&0&0&0&0&0\\ 0&0&0&0&0&0&0&0&0&0&0&0\\ 0&0&0&0&0&0&0&0&0&0&0&0\\ 0&0&0&0&0&0&0&0&0&0&0&0\\ 0&0&0&0&0&0&0&0&0&0.1&0&0\\ 0&0&0&0&0&0&0&0&0&0&0.1&0\\ 0&0&0&0&0&0&0&0&0&0&0&0.1 \end{bmatrix}, R = 55 * \begin{bmatrix} 5.25&0&0&0\\ 0&4.19&0&0\\ 0&0&10.48&0\\ 0&0&0&4 \end{bmatrix} \quad (4.2)$$

Controllability of the system was checked and found to be deficient for both systems. The conventional controllability matrix had a rank of 5 and the tailless controllability matrix had rank 3. Testing stabilizability, both systems were found to be fully stabilizable according to the PBH test of $rank[A - \lambda I \quad B] = n$.

Tables 4.3 and 4.4 present the poles and associated dynamic mode characteristics for the LQR-controlled conventional and modified models. For the conventional model, the LQR controller had little effect on the short period, Dutch roll, and roll modes. The controller significantly increased the damping ratio and natural frequency of the phugoid, making this mode much more stable. The controller also stabilized the spiral mode. Since the controller is mostly controlling the aircraft position, the positional eigenvalues are stabilized and the lateral pair was made complex. The controller had an almost identical effect on the modified model poles, except that it significantly increased the stability of the Dutch roll mode for the modified system.

Between the LQR-controlled systems, most of the dynamic modes are very similar. The modified system has a slightly more stable short period and spiral mode while the conventional system retains a slightly more stable roll mode. Surprisingly, the controlled modified model has Dutch roll and lateral modes with much higher damping ratios than the controlled conventional model. However, the natural frequencies of these modes are still much lower for the modified model.

Table 4.3: Conventional aircraft with LQR state-feedback dynamic mode characteristics

Dynamic Mode	**Pole**	**Damped frequency** ω_D (rad/s)	**Natural frequency** ω_N (rad/s)	**Damping ratio** ζ (-)	**Time constant** $\tau(s)$
Short period	$-10.2726 \pm 8.098i$	8.098	13.0806	0.7853	-
Phugoid	-1.2493 ± 1.2679	1.2679	1.7799	0.7019	-
Dutch Roll	$-0.6442 \pm 6.4414i$	6.4414	6.4735	0.0995	-
Roll	-36.3108	-	-	-	0.0275
Spiral	-1.9837	-	-	-	0.5041
Longitudinal	-0.0979	-	-	-	10.2146
Longitudinal	-0.1068	-	-	-	9.3629
Lateral	-0.9980 ± 1.7208	1.7208	1.9892	0.5017	-

Tables 4.5, 4.6, and 4.7 present controller performance metrics for step offsets. In each of these cases, the model initial condition was set to a 10-meter offset in the east, down, and north direction, respectively, and the controller attempted to return the linear system to trim. In each of these tables, the conventional and modified systems are compared. For all directions, the steady state offset is zero, showing that under these conditions the controller is able to return the system to trim in the long term. Furthermore, the modified system had a slightly lower rise time and settling time than the conventional system, indicating slightly better performance. For the lateral offset, the modified system had an overshoot and decay ratio slightly less than the conventional system, again indicating higher performance. For

Table 4.4: Modified aircraft with LQR state-feedback dynamic mode characteristics

Dynamic Mode	**Pole**	**Damped frequency** ω_D (rad/s)	**Natural frequency** ω_N (rad/s)	**Damping ratio** ζ (-)	**Time constant** $\tau(s)$
Short period	$-10.3431 \pm 7.7275i$	7.7275	12.9110	0.8011	-
Phugoid	$-1.2655 \pm 1.2853i$	1.2853	1.8037	0.7016	-
Dutch Roll	$-1.0275 \pm 1.8257i$	1.8257	2.0950	0.4905	-
Roll	-32.1081	-	-	-	0.0311
Spiral	-2.0583	-	-	-	0.4859
Longitudinal	-0.0985	-	-	-	10.1557
Longitudinal	-0.1062	-	-	-	9.4171
Lateral	-0.2617 ± 0.04314	0.04314	0.2652	0.9867	-

the vertical and longitudinal offsets, the overshoot and decay ratios were nearly equivalent between the two systems. Except for the vertical offset, where the systems were nearly equal, the control effort was less for the modified system than the conventional. The superior performance of the modified system could be the result of multiple differences. One difference is the decreased drag in the modified model, making it easier to accelerate and maneuver with the same thrust. This difference intuitively should affect the vertical and longitudinal performance most. Another difference is that the modified aircraft is able to produce a wider range of force vectors from the empennage due to the rotating tail.

Figure 4.5 shows the system responses in each of the perturbed directions. These graphs support the performance data shown in the tables previously described and give a graphical representation of those metrics. The conventional and modified systems have nearly identical responses in all three directions. However, there is a slight difference in the lateral direction, where the modified system performs slightly faster than the conventional system.

Table 4.5: Controlled model response performance for positive lateral offset (SLUF)

Model	**Steady state offset** (m)	**Rise time** t_r (s)	**Settling time** t_s (s)	**Overshoot ratio** (-)	**Decay ratio** (-)	**Control effort** (-)
Conventional	0.0000	1.7063	3.0347	1.0814	0.1768	350.4456
Modified	0.0000	1.7052	2.7938	1.0028	0.0845	327.1061

Table 4.6: Controlled model response performance for positive vertical offset (SLUF)

Model	**Steady state offset** (m)	**Rise time** t_r (s)	**Settling time** t_s (s)	**Overshoot ratio** (-)	**Decay ratio** (-)	**Control effort** (-)
Conventional	0.0000	8.7292	10.8115	0.9953	0.0262	481.0212
Modified	0.0000	8.6235	10.6920	0.9996	0.0262	481.4841

Table 4.7: Controlled model response performance for negative longitudinal offset (SLUF)

Model	**Steady state offset** (m)	**Rise time** t_r (s)	**Settling time** t_s (s)	**Overshoot ratio** (-)	**Decay ratio** (-)	**Control effort** (-)
Conventional	0.0000	11.0301	11.0301	0.9993	0.0252	538.3539
Modified	0.0000	10.7749	10.7749	0.9993	0.0272	537.4063

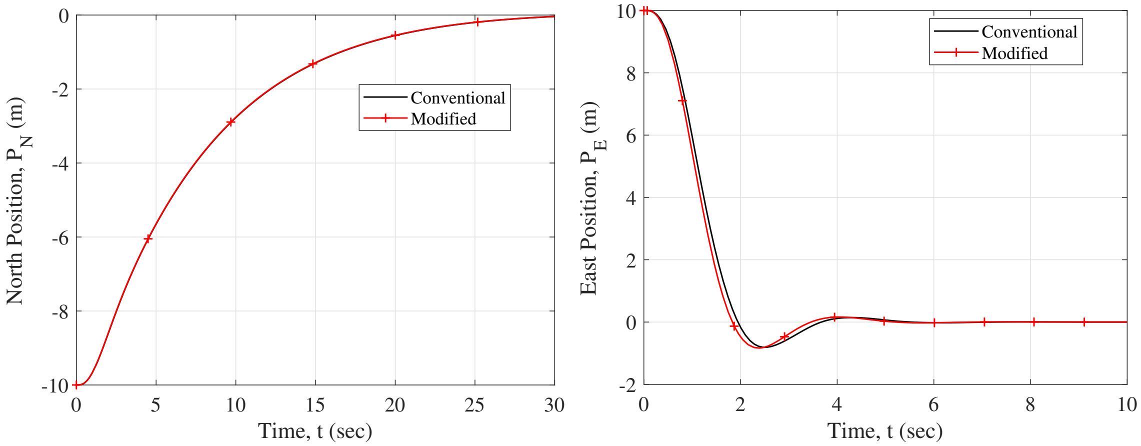

(a) Negative longitudinal offset (b) Positive lateral offset

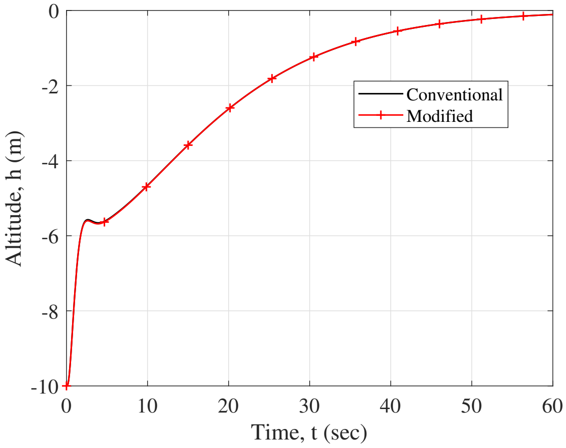

(c) Positive vertical offset

Figure 4.5: LQR-controlled model responses for initial condition perturbations

Figures 4.6, 4.7, and 4.8 show the important control inputs corresponding to the above perturbation responses. This shows that the longitudinal and aileron inputs are generally equivalent between the conventional and modified models, with the only major difference being the trim condition. Figure 4.7b shows that both models rely little on rudder deflection or tail rotation to maneuver.

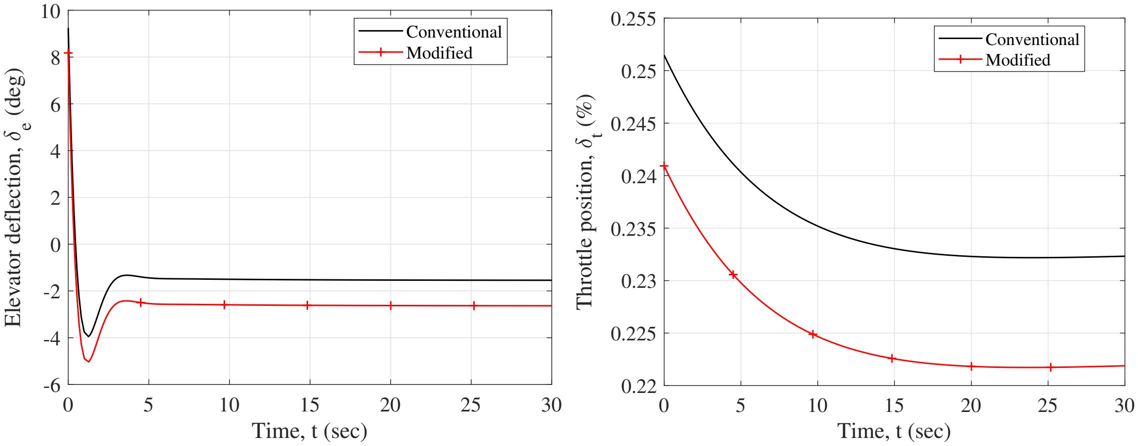

(a) Elevator deflection

(b) Throttle

Figure 4.6: LQR-controlled model control responses for X-position initial condition perturbation

The robustness of a controller to output disturbances can be characterized by the maximum and minimum singular values of the output closed-loop transfer function, $L_o(j\omega)$. The singular values for both the conventional and modified systems over a range of frequencies are compared in Figure 4.9a. The minimum singular values of the modified system tend to be greater than the conventional system at low frequencies, indicating better performance robustness. The modified maximum singular values appear to be larger for mid-range frequencies and near equivalent to the conventional system at low and high frequencies, indicating worse stability robustness. However, both systems have very small minimum singular values across most frequencies, which results in extremely large condition numbers shown

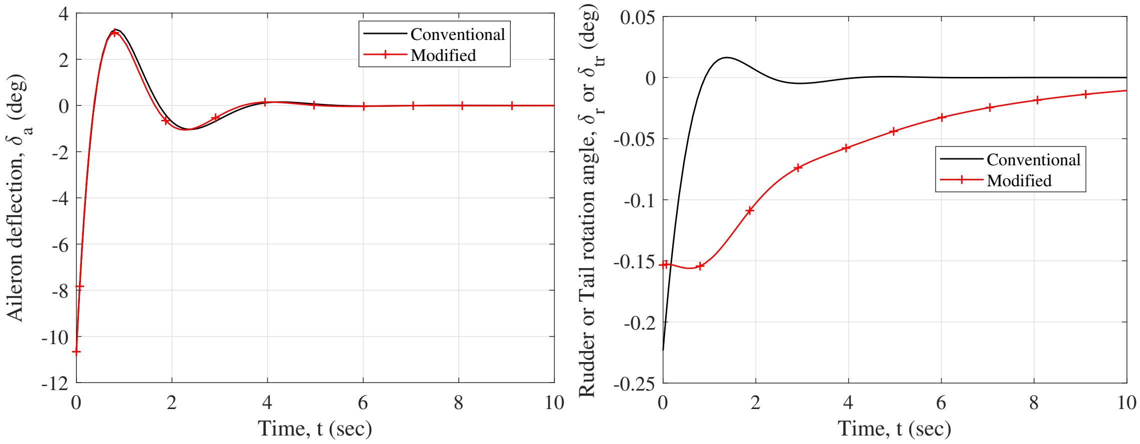

(a) Aileron deflection

(b) Rudder deflection

Figure 4.7: LQR-controlled model control responses for Y-position initial condition perturbation

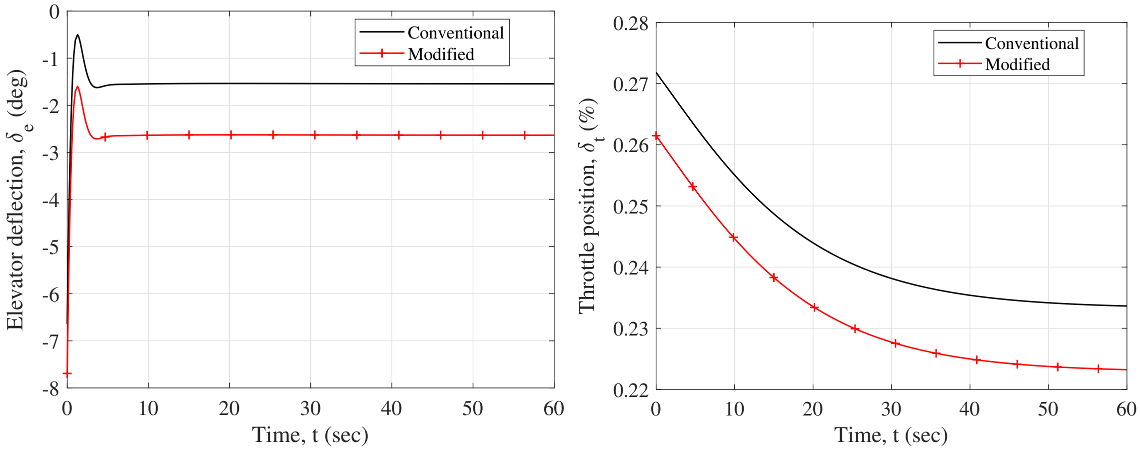

(a) Elevator deflection

(b) Throttle

Figure 4.8: LQR-controlled model control responses for Z-position initial condition perturbation

in Figure 4.9b. This indicates severely limited robustness for both systems, which as shown later is not necessarily the case.

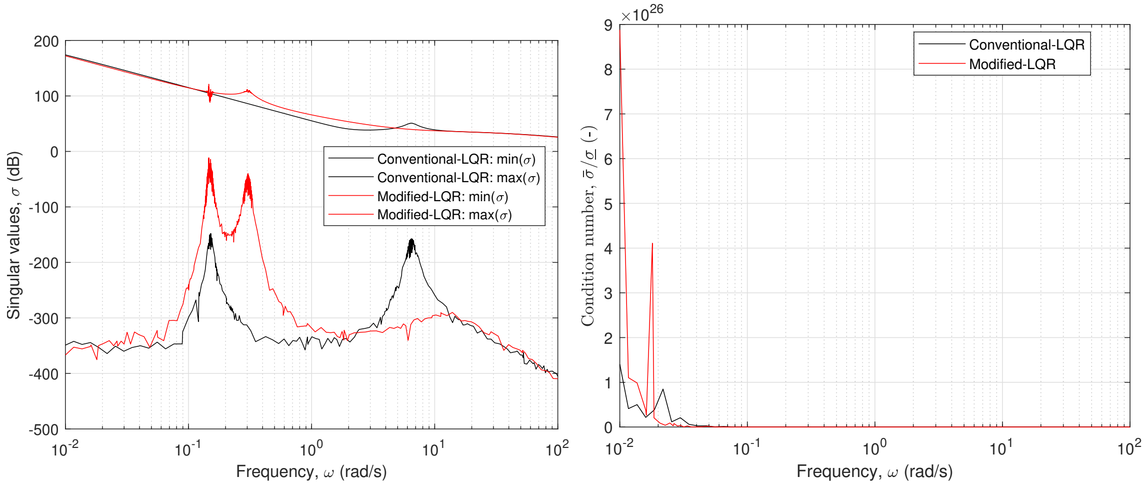

(a) Maximum and minimum singular values

(b) Condition number

Figure 4.9: LQR-controlled system output closed-loop transfer matrix singular values

Similarly, the singular values of the input closed-loop transfer matrix, $L_i(j\omega)$, can describe robustness to input perturbations. Figure 4.10a shows the maximum and minimum singular values for the LQR-controlled systems. The maximum singular values tend to be nearly equivalent between the systems, but the modified system tends to have greater minimum singular values across frequencies, which indicates better performance robustness. This trend is further shown in the higher condition number of the conventional system, shown in Figure 4.10b.

The maximum singular values of the sensitivity functions also give insights to the robustness of the systems. The output sensitivity function maximum singular values are shown in Figure 4.11a, which corresponds to output disturbance rejection performance. At low frequencies, the conventional system singular values are less than the modified system, indicating better performance. The output complementary sensitivity functions are shown in

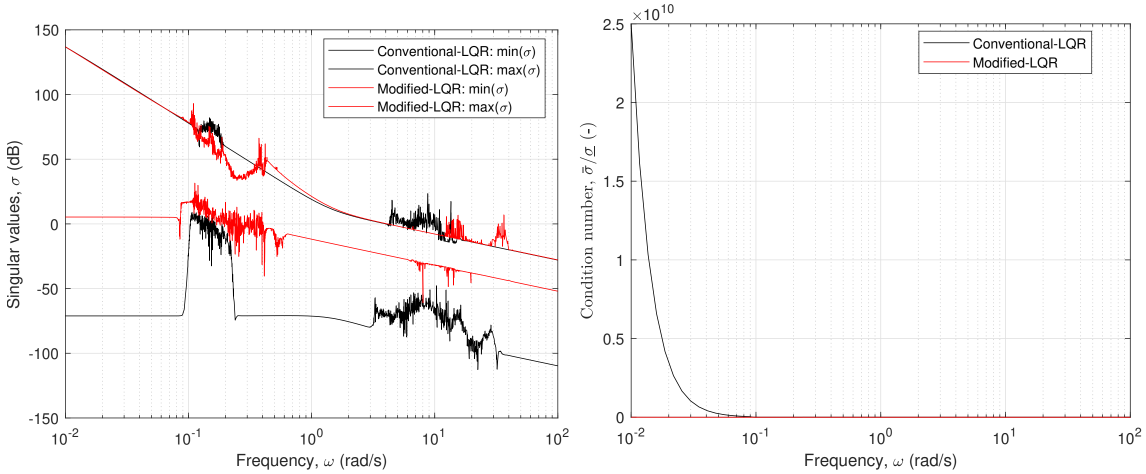

(a) Maximum and minimum singular values

(b) Condition number

Figure 4.10: LQR-controlled system input closed-loop transfer matrix singular values

Figure 4.11b, which indicates similar output noise rejection properties, since the systems are fairly equal at high frequencies. However, the conventional system shows worse robustness with a spike at around 6-7 rad/s. Figure 4.12a shows the input sensitivity singular values for both systems. At very low frequencies, the modified system singular values are larger than the conventional system, indicating worse input disturbance rejection. Figure 4.12b shows the singular values of the input complementary sensitivity function, which are nearly equivalent between systems at high frequencies and thus nearly equivalent input noise rejection.

In addition to the above metrics, the A-matrix for both systems was directly perturbed and the stability of the system was evaluated by looking at the eigenvalues. Only positions (2,2), (2,4), (4,2), (4,4), (4,6), (6,2), (6,4), and (6,6) in the A-matrix were perturbed. These positions correspond to interactions between the states v (side velocity), p (roll rate), and r (yaw rate) and were chosen because intuitively and in actuality these values showed the most difference between the conventional and modified systems and are the most uncertain for the modified model. The perturbations applied were random Gaussian addition to the

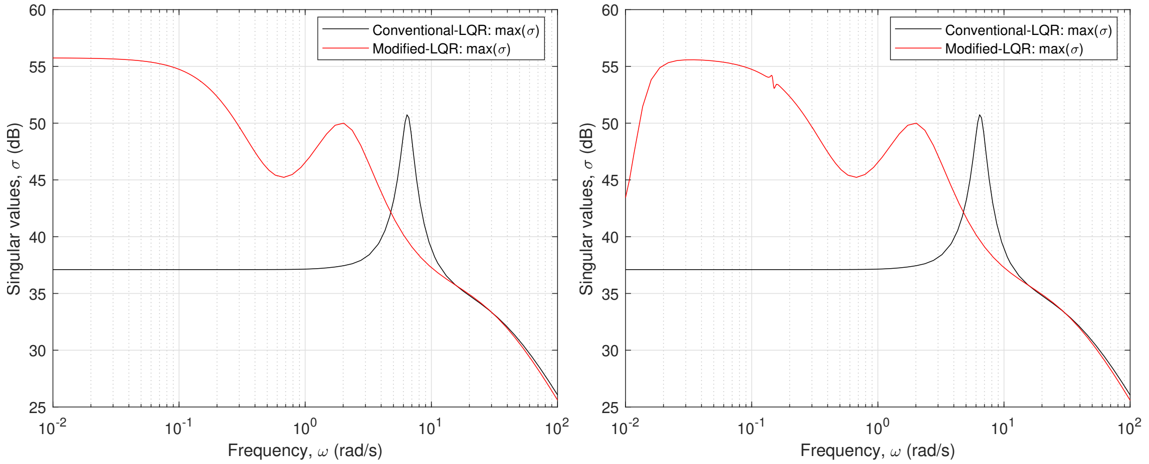

(a) Sensitivity function (b) Cosensitivity function

Figure 4.11: Maximum singular values of the output sensitivity functions

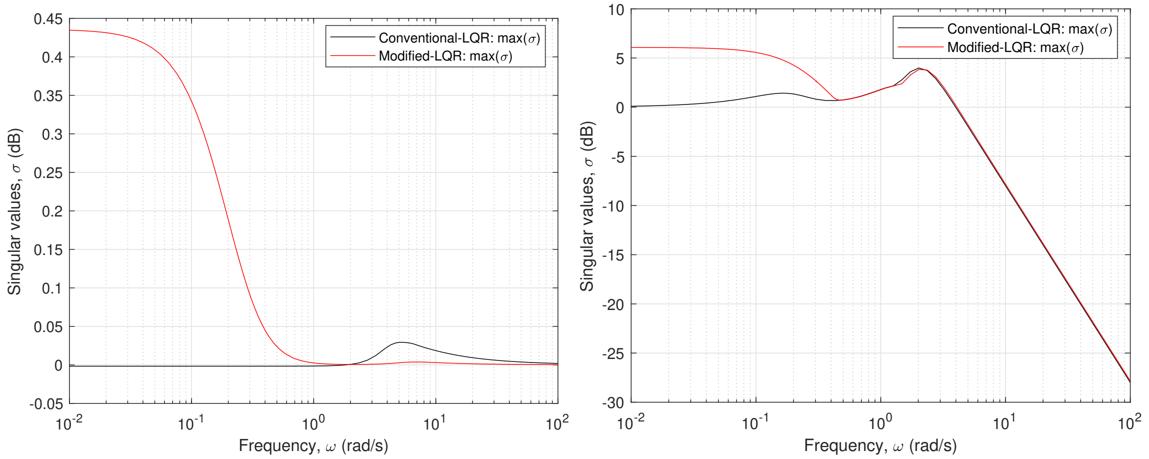

(a) Sensitivity function (b) Cosensitivity function

Figure 4.12: Maximum singular values of the input sensitivity functions

chosen positions of a percentage of the actual model value. Many iterations were done and the maximum percentage was reduced until none of the iterations resulted in an unstable system. Using this process, it was found that the conventional system could tolerate ±30.4% perturbations in the A-matrix in the chosen positions before possibly going unstable, while the modified system could tolerate only ±2.7% perturbations. Therefore, although both systems showed similar time-domain performance, the modified system is much less robust to system uncertainties than the conventional system.

4.4 Guaranteed-Cost Control

Using the polytopic uncertainty principle, a guaranteed-cost controller was designed for the same system and trim condition of straight, level, unaccelerated flight. In order to better show the differences from the LQR solution and between the conventional and modified systems, the controller was designed such that the system is guaranteed to remain stable with up to 50 percent perturbations in the following A-matrix positions: (2,2), (2,4), (4,2), (4,4), (4,6), (6,2), (6,4), and (6,6). As explained above, these channels are intuitively where the largest uncertainties lie.

The poles, natural frequencies, and damping ratios for the conventional and modified systems with this controller are shown in Tables 4.8 and 4.9, respectively. With this controller, all modes are stabilized. Unlike the LQR controller, the guaranteed-cost controller has made all the poles of both systems complex. The short period, phugoid, and longitudinal modes are nearly identical between the two configurations. The spiral mode of the conventional system has a slightly greater damping ratio and natural frequency than the modified system. The modified roll mode has a higher natural frequency and lower damping ratio than the conventional system. Similar to the LQR system, the modified Dutch roll mode has a higher damping ratio than the conventional system, but a much lower natural frequency. Interestingly, this controller increased the conventional Dutch roll mode damping ratio more than the LQR controller.

Table 4.10 compares the time domain performance of the conventional and modified

Table 4.8: Poles of the conventional aircraft with guaranteed-cost state-feedback

Dynamic Mode	**Pole**	**Damped frequency** ω_D (rad/s)	**Natural frequency** ω_N (rad/s)	**Damping ratio** ζ (-)
Short Period	$-10.2726 \pm 8.0978i$	8.0978	13.0806	0.7853
Phugoid	$-1.2493 \pm 1.2679i$	1.2679	1.7799	0.7019
Dutch Roll	$-4.1729 \pm 7.2047i$	7.2047	8.3259	0.5012
Spiral	-0.3342 ± 0.3561	0.3561	0.4883	0.6843
Roll	$-28.1478 \pm 17.7951i$	17.7951	33.3011	0.8453
Longitudinal	$-0.1772 \pm 0.1445i$	0.1445	0.2287	0.7749

Table 4.9: Poles of the modified aircraft with guaranteed-cost state-feedback

Dynamic Mode	**Pole**	**Damped frequency** ω_D (rad/s)	**Natural frequency** ω_N (rad/s)	**Damping ratio** ζ (-)
Short Period	$-10.3431 \pm 7.7275i$	7.7275	12.9110	0.8011
Phugoid	-1.2655 ± 1.2853	1.2853	1.8037	0.7016
Dutch Roll	$-1.4031 \pm 1.1417i$	1.1417	1.8089	0.7757
Spiral	$-0.2092 \pm 0.2394i$	0.2394	0.3179	0.6579
Roll	$-36.0477 \pm 30.3729i$	30.3729	47.1376	0.7647
Longitudinal	$-0.1772 \pm 0.1445i$	0.1445	0.2287	0.7748

systems with respect to a 10-meter positive lateral initial condition offset. The conventional system outperforms the modified system in every metric, having a more than 2-second faster rise time, a roughly 6-second faster settling time, slightly better overshoot and decay ratios, and with less control effort. This was not the case with the LQR controller, where the conventional and modified system performance was nearly equivalent. Figure 4.14 shows this difference in performance and compares it to the LQR-controlled systems. In this figure, the conventional and modified LQR systems follow nearly identical paths in their east position. The guaranteed-cost systems both approach the desired position more slowly than the LQR systems, and the modified guaranteed-cost system is significantly slower to converge than the conventional system. It is expected that the guaranteed-cost system performance is less than the LQR performance, since in order to increase the robustness of the system, convergence speed must be sacrificed. It also appears that to make the conventional and modified systems have the same robustness, the performance of the modified system must be sacrificed.

Tables 4.11 and 4.12 show the performance of the guaranteed-cost controllers for a positive vertical and negative longitudinal 10-meter initial condition offset. For these cases, the conventional and modified systems performed almost the same, which is expected since the rotating horizontal tail has little effect on the longitudinal dynamics. However, the conventional system did require less control effort than the modified system, which differs from the LQR-controlled system results. Graphs of the position response for all these cases are found in Figure 4.13.

Figures 4.15, 4.16, and 4.17 show the important control inputs corresponding to the above perturbation responses. Just as with the LQR controller, the longitudinal inputs are generally equivalent between the conventional and modified models. However, Figures 4.16a and 4.16b show greater aileron and rudder deflections and more abrupt movements. Furthermore, the greater control effort can be seen in these graphs, since the modified model tends to have larger aileron and tail rotation deflections than the conventional configuration.

Figure 4.18a shows the singular values of the output closed-loop transfer matrix, while Figure 4.18b shows the condition number. This metric is nearly identical to the LQR-

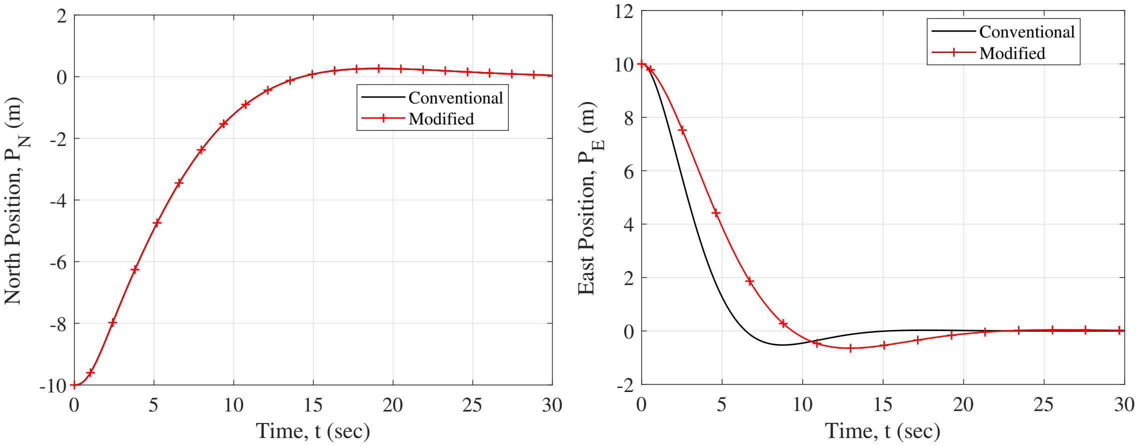

(a) Negative longitudinal offset

(b) Positive lateral offset

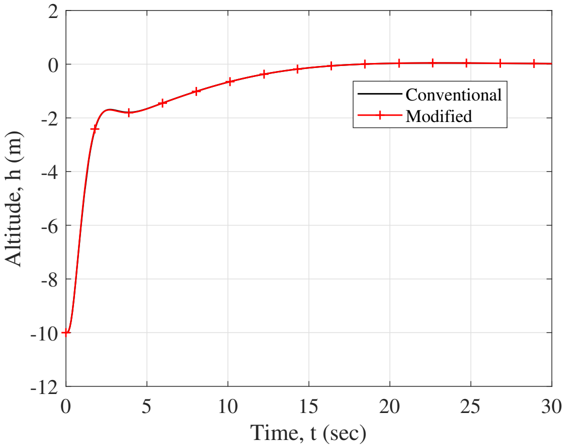

(c) Positive vertical offset

Figure 4.13: guaranteed-cost-controlled model responses for initial condition perturbations

Table 4.10: guaranteed-cost controlled model response performance for positive lateral offset (SLUF)

Model	**Steady state offset** (m)	**Rise time** t_r (s)	**Settling time** t_s (s)	**Overshoot ratio** (-)	**Decay ratio** (-)	**Control effort** (-)
Conventional	0.0000	5.3266	9.4008	1.0028	0.0527	102.8157
Modified	0.0000	7.7544	15.4129	1.0645	0.0645	149.6715

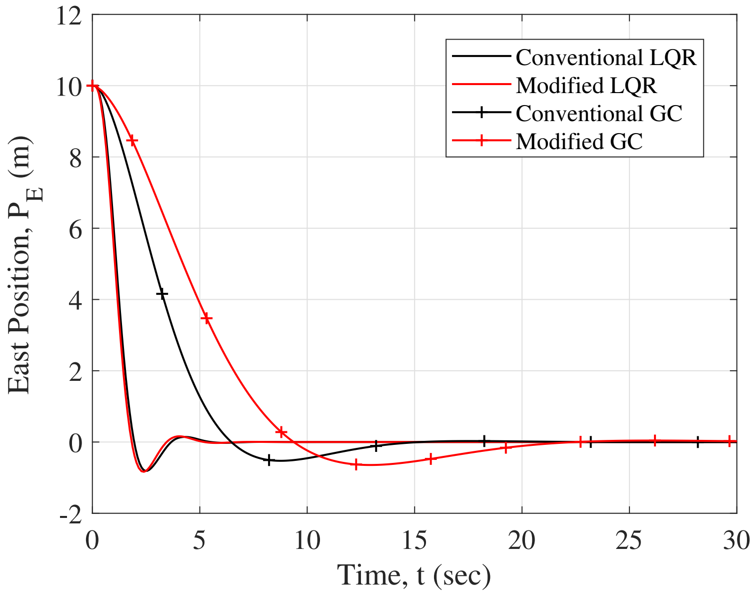

Figure 4.14: Simulated trajectory comparing the response to a 10 meter perturbed initial condition for both systems with LQR and guaranteed-cost controllers

Table 4.11: guaranteed-cost controlled model response performance for positive vertical offset (SLUF)

Model	**Steady state offset** (m)	**Rise time** t_r (s)	**Settling time** t_s (s)	**Overshoot ratio** (-)	**Decay ratio** (-)	**Control effort** (-)
Conventional	0.0000	8.1994	11.1560	1.0045	0.0253	185.2750
Modified	0.0000	8.1757	11.1675	1.0046	0.0253	234.4838

Table 4.12: guaranteed-cost controlled model response performance for negative longitudinal offset (SLUF)

Model	**Steady state offset** (m)	**Rise time** t_r (s)	**Settling time** t_s (s)	**Overshoot ratio** (-)	**Decay ratio** (-)	**Control effort** (-)
Conventional	0.0000	10.5583	11.8823	0.9734	0.0212	168.8415
Modified	0.0000	10.5424	11.8685	0.9734	0.0213	204.4579

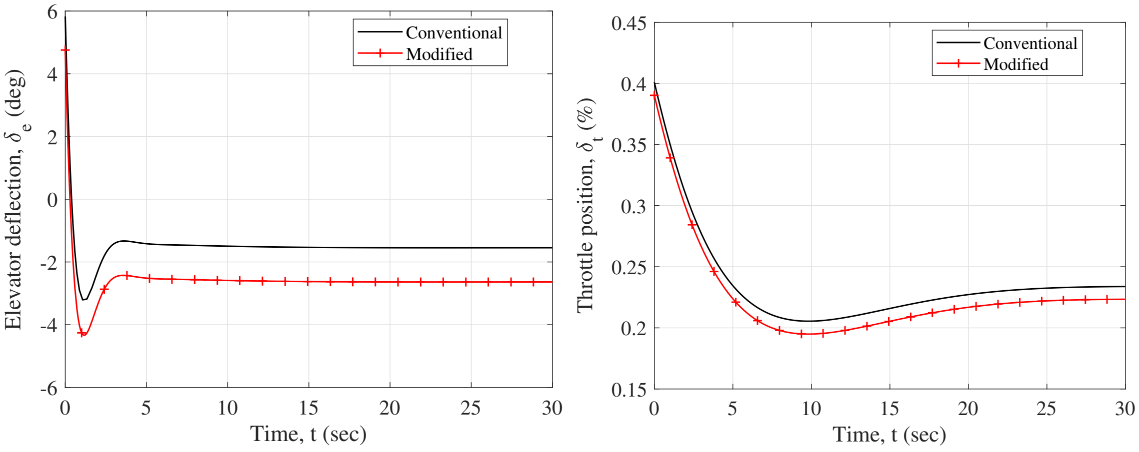

(a) Elevator deflection (b) Throttle

Figure 4.15: guaranteed-cost-controlled model control responses for X-position initial condition perturbation

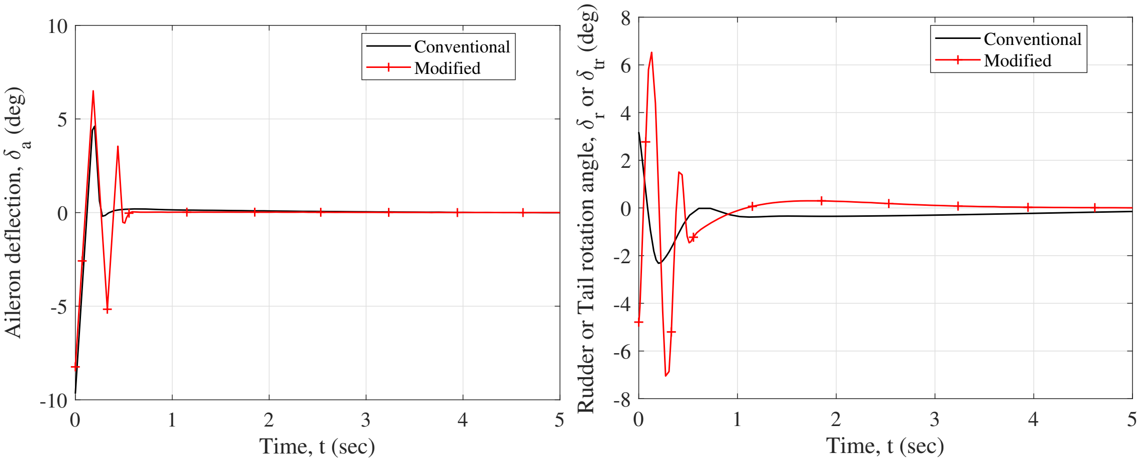

(a) Aileron deflection (b) Rudder deflection

Figure 4.16: guaranteed-cost-controlled model control responses for Y-position initial condition perturbation

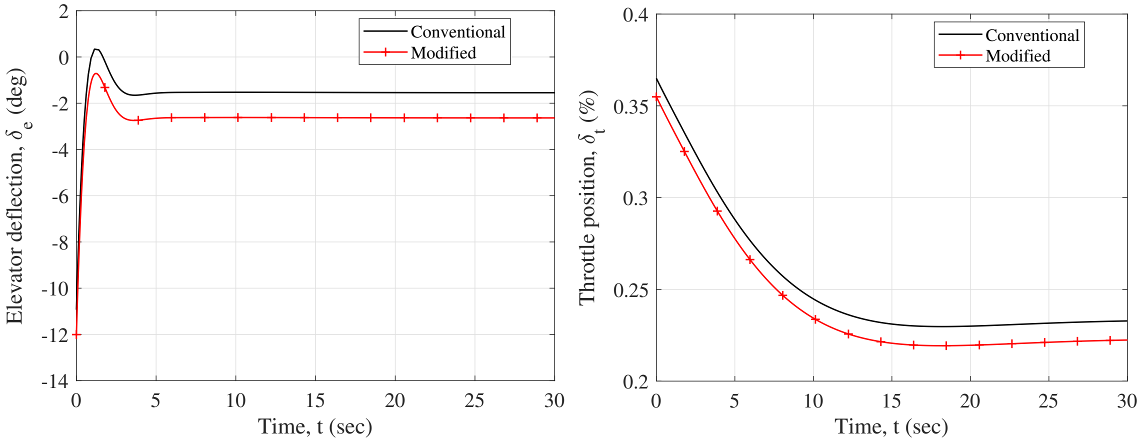

(a) Elevator deflection

(b) Throttle

Figure 4.17: guaranteed-cost-controlled model control responses for Z-position initial condition perturbation

controlled systems. However, the input closed-loop transfer matrix singular values and condition number, shown in Figure 4.19, indicates very similar input perturbation robustness, except for higher minimum singular values for the modified system at low frequencies indicating better performance robustness.

The output sensitivity function singular values in Figure 4.20a are greater at low frequencies for the modified system, indicating better output disturbance rejection, while the cosensitivity functions in Figure 4.20b are nearly equal at high frequencies, indicating similar output noise rejection. The input sensitivity and cosensitivity functions, shown in Figure 4.21, show the opposite trends, meaning the conventional system has better input disturbance rejection and worse input noise rejection.

Using the same process as for the LQR-controlled system, the guaranteed-cost-controlled system A-matrix was directly perturbed and the maximum tolerable perturbation before the system went unstable was found. The maximum tolerable perturbation for the conventional system is roughly 107.3 percent, while for the modified system it is about 131.6 percent.

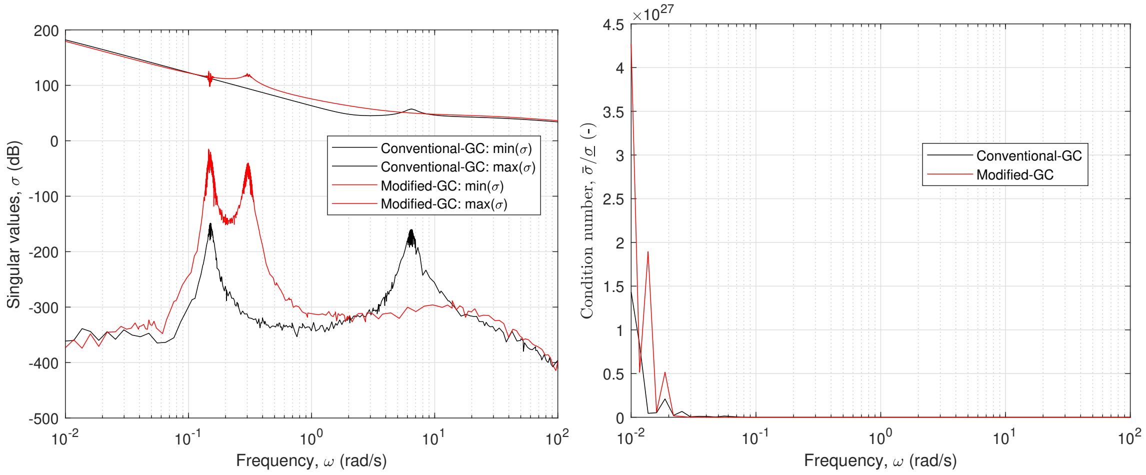

(a) Maximum and minimum singular values (b) Condition number

Figure 4.18: guaranteed-cost-controlled system output closed-loop transfer matrix singular values

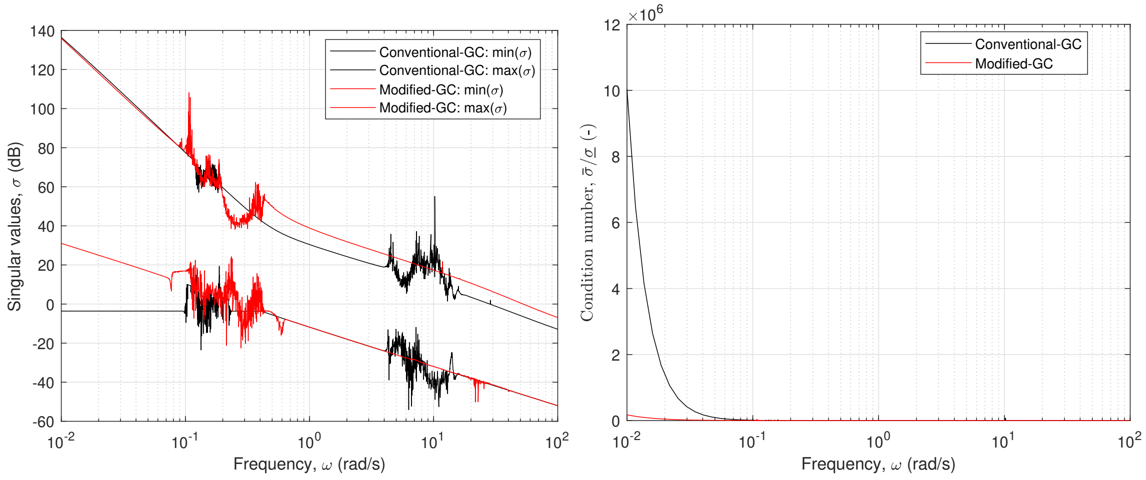

(a) Maximum and minimum singular values (b) Condition number

Figure 4.19: guaranteed-cost-controlled system input closed-loop transfer matrix singular values

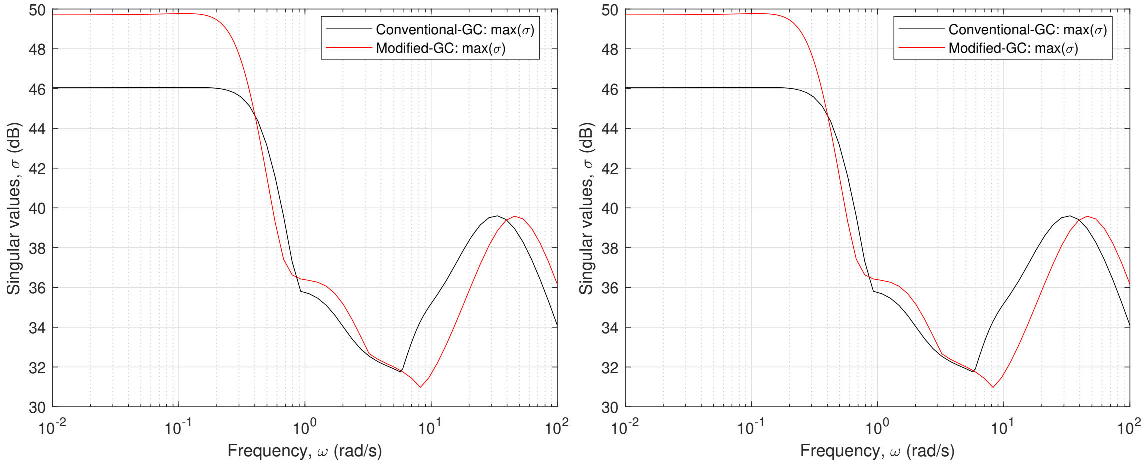

(a) Sensitivity function

(b) Cosensitivity function

Figure 4.20: Maximum singular values of the output sensitivity functions for the guaranteed-cost-controlled system

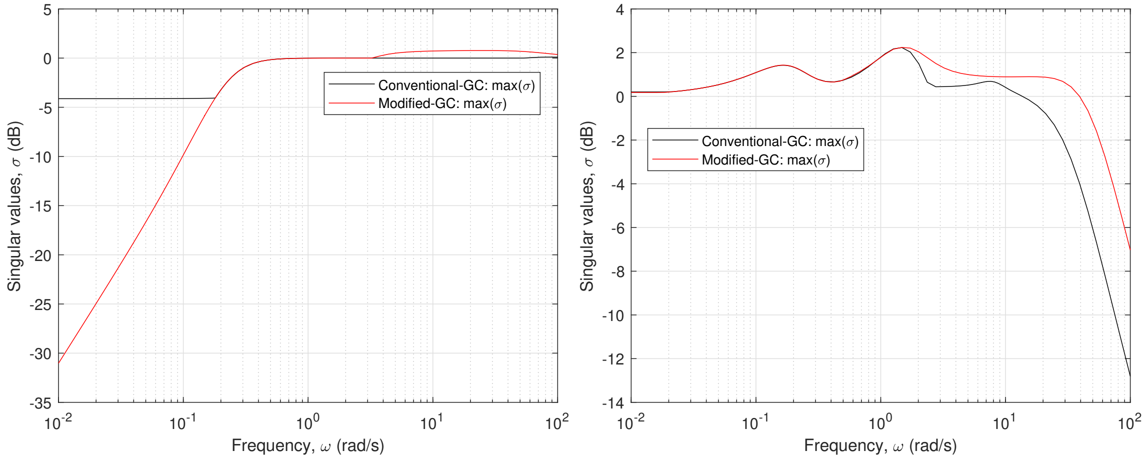

(a) Sensitivity function

(b) Cosensitivity function

Figure 4.21: Maximum singular values of the input sensitivity functions for the guaranteed-cost-controlled system

While these numbers are stochastic estimates, they show that the guaranteed-cost systems are much more tolerant of uncertainty in the A-matrix than the LQR systems, and that the guaranteed-cost solution successfully improved the robustness of the modified system significantly.

4.4.1 A and B Matrix Perturbations

Using the same method as above, another guaranteed-cost controller was designed to guarantee stability for the perturbed system with additional perturbations to the B-matrix in positions (2,3), (4,3), and (6,3). These positions correspond to the influence of rudder or tail rotation control inputs on the side velocity (v), roll rate (p), and yaw rate (r). These positions showed the greatest difference between the conventional and modified systems and are likely the most uncertain for the modified system.

Tables 4.13 and 4.14 show the dynamic mode poles and characteristics for the conventional and modified systems controlled with the augmented guaranteed-cost controller. The longitudinal modes remain nearly unchanged from the base guaranteed-cost systems and are very similar between the conventional and modified systems. The spiral and roll modes changed slightly with the augmentation, but are still complex and stable with similar natural frequencies and damping ratios. Interestingly, the Dutch roll mode poles became real and stable for both configurations. A possible explanation for this could be that since the augmented controller is less aggressive, resulting in no overshoots and is thus non-oscillatory in the Dutch roll, causing the complex Dutch roll pole to be split into two real and stable poles. The other pole that may correspond to the Dutch roll mode is labelled as the Lat-Dir mode, for which the eigenvector also corresponded to the lateral-directional states.

Tables 4.16 and 4.17 present the numerical time domain performance data for a 10-meter initial condition offset in the vertical and longitudinal directions, respectively. Similar to the baseline guaranteed-cost system, there is very little difference between the conventional and modified systems, except for the conventional system requiring less control effort. Table 4.15 presents the time domain performance for a lateral offset, which, like the baseline

Table 4.13: Conventional aircraft with augmented guaranteed-cost state-feedback

Dynamic Mode	**Pole**	**Damped frequency** ω_D (rad/s)	**Natural frequency** ω_N (rad/s)	**Damping ratio** ζ (-)	**Time constant** τ (s)
Short Period	$-10.2726 \pm 8.0978i$	8.0978	13.0806	0.7853	-
Phugoid	$-1.2493 \pm 1.2679i$	1.2679	1.7799	0.7019	-
Dutch Roll	-6.6921	-	-	-	0.1494
Spiral	$-0.2030 \pm 0.2003i$	0.2003	0.2852	0.7117	-
Roll	$-47.8836 \pm 30.8300i$	30.8300	56.9503	0.8408	-
Longitudinal	$-0.1772 \pm 0.1445i$	0.1445	0.2287	0.7749	-
Lat-Dir	-18.2660	-	-	-	0.0547

Table 4.14: Modified aircraft with augmented guaranteed-cost state-feedback poles

Dynamic Mode	**Pole**	**Damped frequency** ω_D (rad/s)	**Natural frequency** ω_N (rad/s)	**Damping ratio** ζ (-)	**Time constant** τ (s)
Short Period	$-10.3431 \pm 7.7275i$	7.7275	12.9110	0.8011	-
Phugoid	$-1.2655 \pm 1.2853i$	1.2853	1.8037	0.7016	-
Dutch Roll	-1.4694	-	-	-	0.6806
Spiral	$-0.1415 \pm 0.1624i$	0.2394	0.3179	0.6579	-
Roll	$-48.7143 \pm 47.2771i$	47.2771	67.8838	0.7176	-
Longitudinal	$-0.1772 \pm 0.1445i$	0.1445	0.2287	0.7748	-
Lat-Dir	-6.0639	-	-	-	0.1649

guaranteed-cost system, shows that the modified system response is significantly slower than the conventional system. Furthermore, the control effort required is more than four times as much for the modified system. Figure 4.22 supports this data with the graphs of the positional responses to each of these cases.

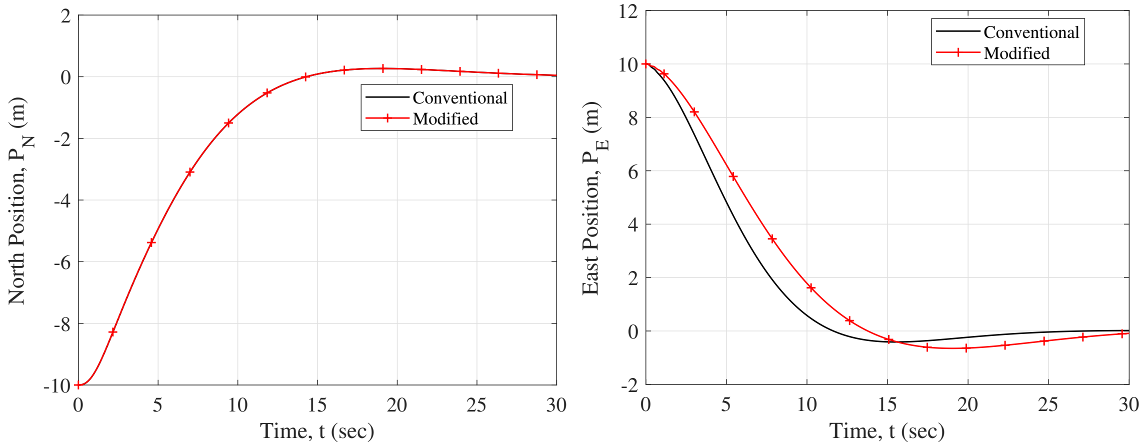

(a) Negative longitudinal offset (b) Positive lateral offset

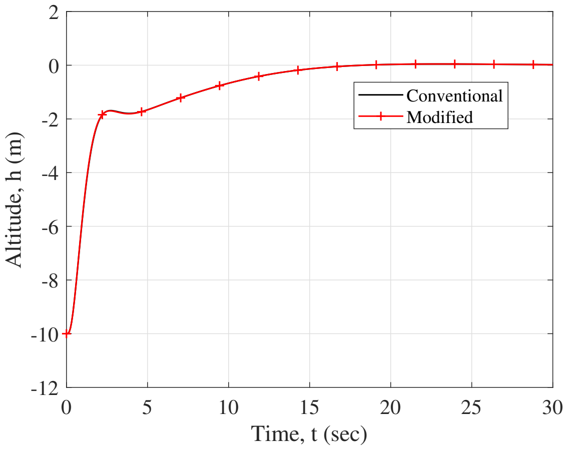

(c) Positive vertical offset

Figure 4.22: Augmented guaranteed-cost-controlled model responses for initial condition perturbations

Figures 4.23, 4.24, and 4.25 show the important control inputs corresponding to the

Table 4.15: Augmented guaranteed-cost controlled model response performance for positive lateral offset (SLUF)

Model	**Steady state offset** (m)	**Rise time** t_r (s)	**Settling time** t_s (s)	**Overshoot ratio** (-)	**Decay ratio** (-)	**Control effort** (-)
Conventional	0.0000	9.2117	10.1436	1.0412	0.0412	157.7274
Modified	0.0000	11.3528	22.8244	1.0651	0.0651	683.3899

Table 4.16: Augmented guaranteed-cost controlled model response performance for positive vertical offset (SLUF)

Model	**Steady state offset** (m)	**Rise time** t_r (s)	**Settling time** t_s (s)	**Overshoot ratio** (-)	**Decay ratio** (-)	**Control effort** (-)
Conventional	0.0000	8.1416	11.1760	1.0045	0.0253	261.8042
Modified	0.0000	8.1301	11.1429	1.0046	0.0253	304.7892

Table 4.17: Augmented guaranteed-cost controlled model response performance for negative longitudinal offset (SLUF)

Model	**Steady state offset** (m)	**Rise time** t_r (s)	**Settling time** t_s (s)	**Overshoot ratio** (-)	**Decay ratio** (-)	**Control effort** (-)
Conventional	0.0000	10.5118	11.9217	0.9734	0.0212	223.2730
Modified	0.0000	10.5247	11.8834	0.9734	0.0213	255.9743

above perturbation responses. The trend of greater and more abrupt deflections continues in Figures 4.16a and 4.16b, which especially show the much greater control effort of the modified system.. Furthermore, unlike the LQR-controlled systems, the majority of the control inputs for the lateral perturbation return to zero after only a few seconds and have long-lasting effects on the system response.

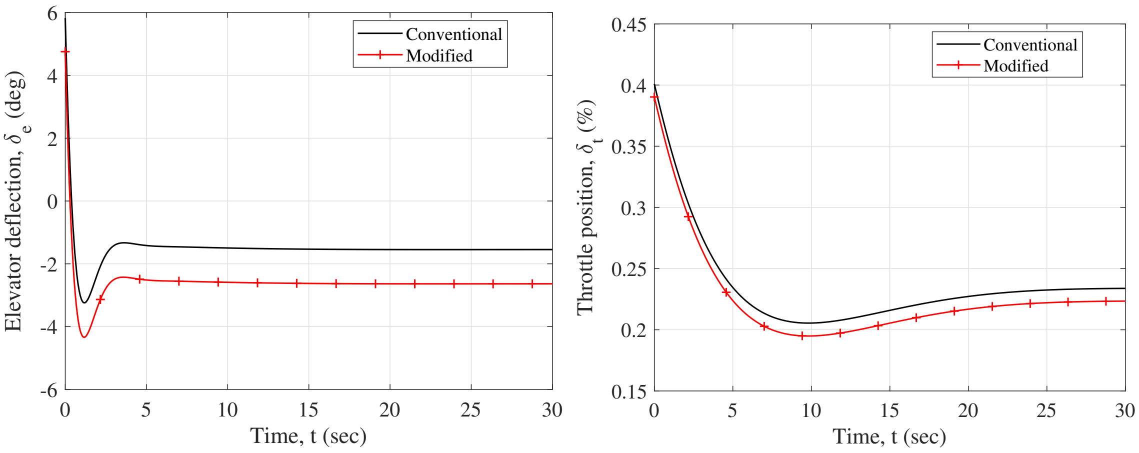

(a) Elevator deflection (b) Throttle

Figure 4.23: Augmented guaranteed-cost-controlled model control responses for X-position initial condition perturbation

Figure 4.26a shows the singular values of the output closed-loop transfer matrix, while Figure 4.26b shows the condition number. This metric is nearly identical to the LQR- and baseline guaranteed-cost-controlled systems. However, the input closed-loop transfer matrix singular values and condition number, shown in Figure 4.27, indicates more similar input perturbation robustness between the configurations with an increase in the conventional minimum singular values at low frequencies compared to the baseline guaranteed-cost system.

The output and input sensitivity function singular values, found in Figures 4.28 and 4.29 respectively, show nearly identical trends as the baseline guaranteed-cost system. In general, the conventional and modified systems became more similar in their sensitivity function

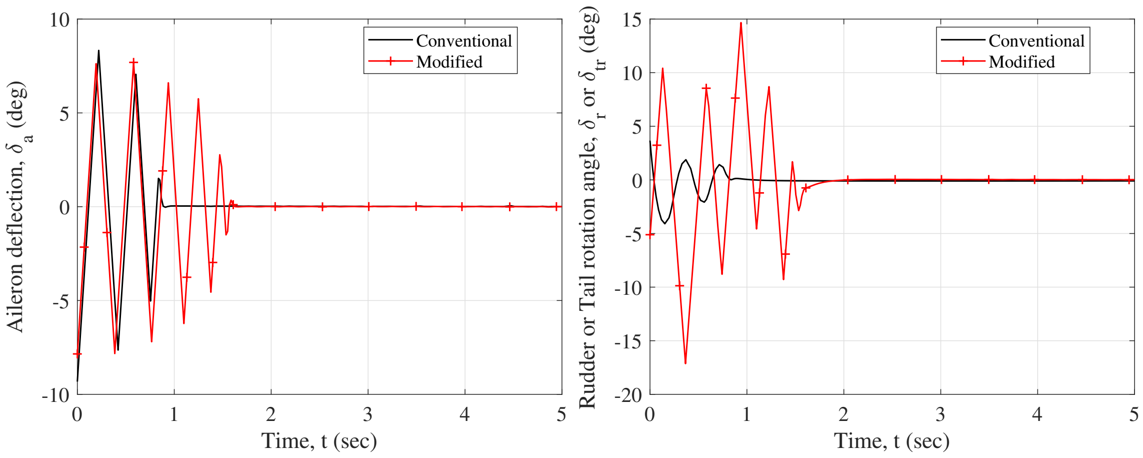

(a) Aileron deflection

(b) Rudder deflection

Figure 4.24: Augmented guaranteed-cost-controlled model control responses for Y-position initial condition perturbation

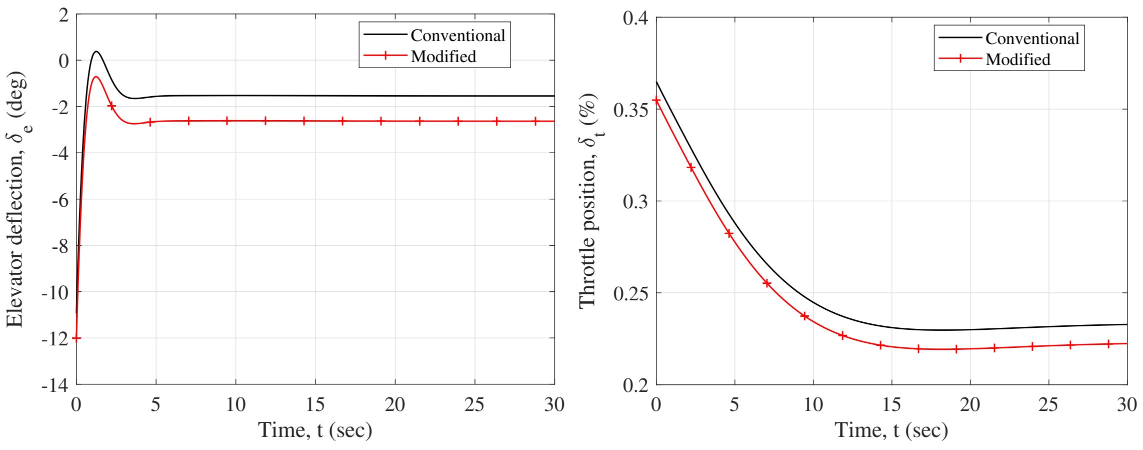

(a) Elevator deflection

(b) Throttle

Figure 4.25: Augmented guaranteed-cost-controlled model control responses for Z-position initial condition perturbation

singular values with the augmentation of the controller.

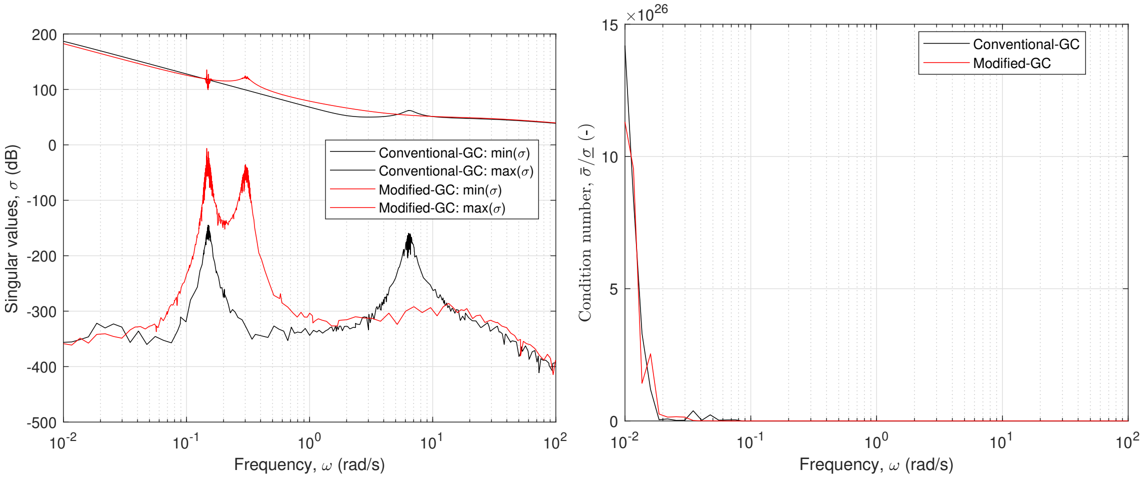

(a) Maximum and minimum singular values

(b) Condition number

Figure 4.26: Augmented guaranteed-cost-controlled system output closed-loop transfer matrix singular values

Using the same process as before, the augmented guaranteed-cost-controlled system A-matrix was directly perturbed and the maximum tolerable perturbation before the system went unstable was found. The maximum tolerable perturbation for the conventional system is roughly 213.0 percent, while for the modified system it is about 300.7 percent. This is a huge increase from the baseline guaranteed-cost controller, nearly double for the conventional system and more than double for the modified system.

The same analysis was repeated, except with perturbations applied to both the A- and B-matrices. The same positions of the A-matrix were perturbed as before, and the B-matrix was perturbed in positions (2,3), (4,3), and (6,3), corresponding to the positions of greatest difference and uncertainty. The maximum tolerable perturbation to both the A- and B-matrices for the conventional augmented guaranteed-cost-controlled system was 66.3 percent, while for the modified system it was 66.4 percent. The same A- and B-matrix perturbations

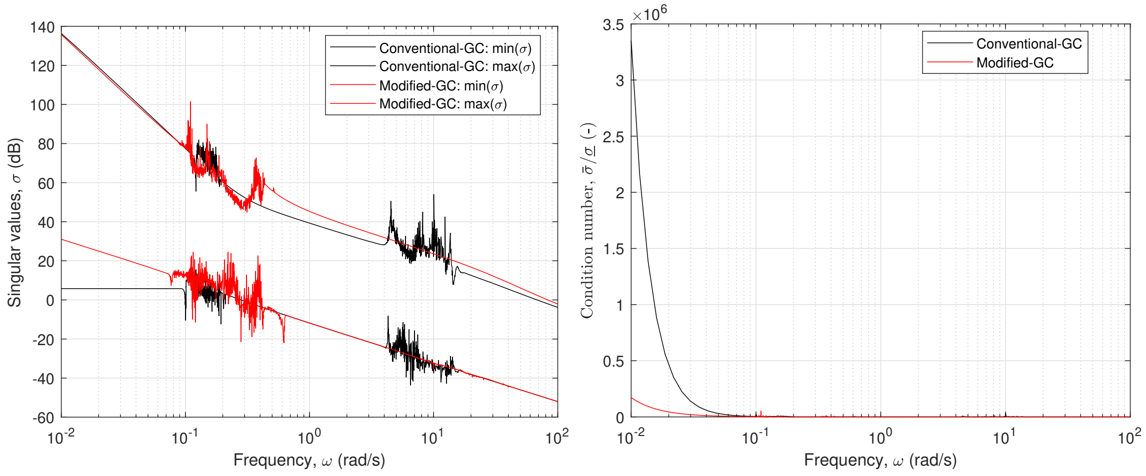

(a) Maximum and minimum singular values

(b) Condition number

Figure 4.27: Augmented guaranteed-cost-controlled system input closed-loop transfer matrix singular values

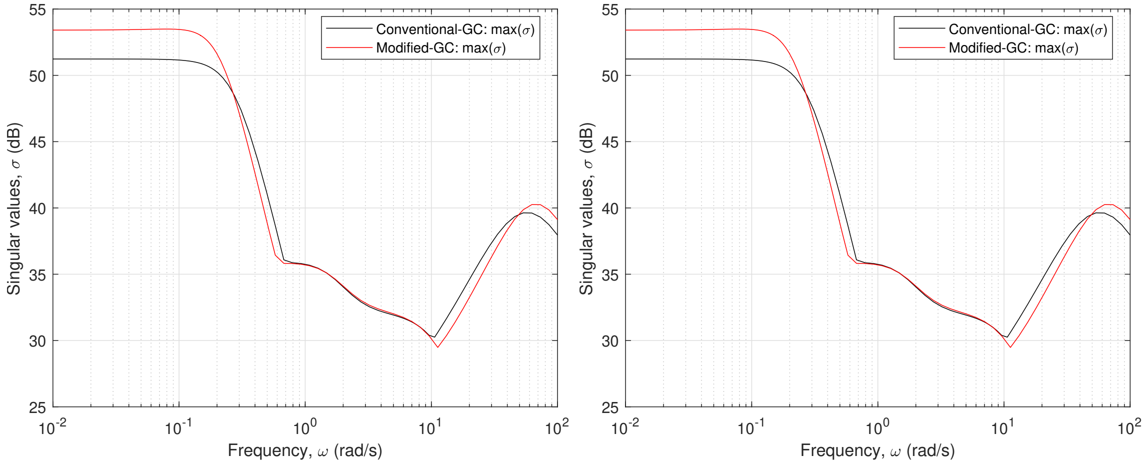

(a) Sensitivity function

(b) Cosensitivity function

Figure 4.28: Maximum singular values of the output sensitivity functions for the augmented guaranteed-cost-controlled system

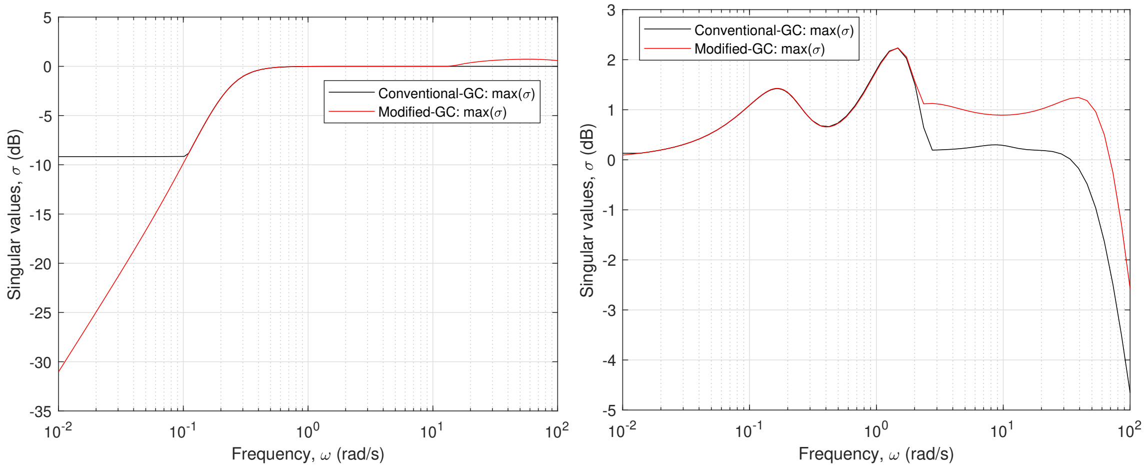

(a) Sensitivity function

(b) Cosensitivity function

Figure 4.29: Maximum singular values of the input sensitivity functions for the augmented guaranteed-cost-controlled system

were applied to the LQR and guaranteed-cost systems. The maximum tolerable perturbation for the conventional LQR-controlled system was found to be 30.4 percent, and 2.6 percent for the modified system. Likewise, for the guaranteed-cost systems the tolerable perturbation was found to be 59.8 percent for the conventional system and 50.4 percent for the modified system. While the baseline guaranteed-cost systems are surprisingly robust to B-matrix perturbations, the augmentation did result in increased robustness.

Figure 4.30 presents a comparison of the position responses of the LQR, guaranteed-cost, and augmented guaranteed-cost systems. These graphs again show that the increased robustness of the guaranteed-cost controller sacrificed the time domain performance of the LQR systems in the lateral axis. However, the augmented guaranteed-cost system performed nearly identical to the base guaranteed-cost system in the longitudinal axes (x and z) and faster than the LQR system. This is likely because the only difference in the augmented system was that it was designed for uncertainty in the rudder and tail rotation control effects on the lateral-directional states. For the offset in the East position, the augmented system followed the trend of a slower response with the increased robustness. Furthermore, the difference in performance between the conventional and modified systems with the augmented controller is similar to the differences found in the base guaranteed-cost controlled systems.

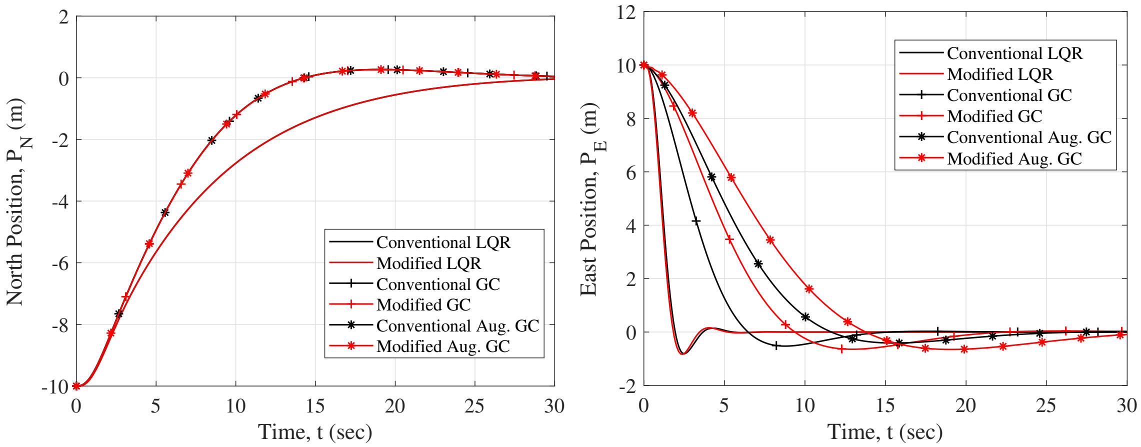

(a) Negative longitudinal offset

(b) Positive lateral offset

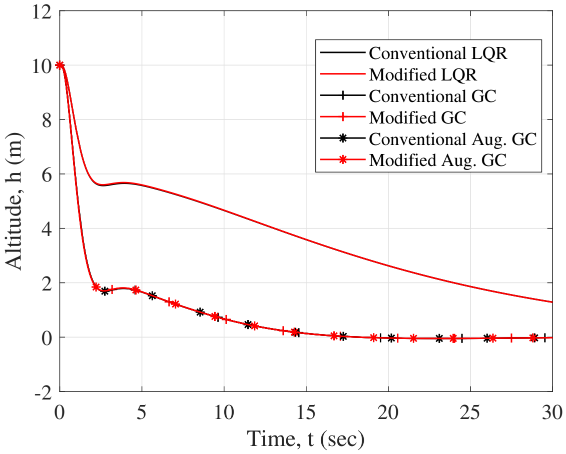

(c) Positive vertical offset

Figure 4.30: Augmented guaranteed-cost-controlled model responses for initial condition perturbations

Chapter 5

CONCLUSION

As demand continues to drive increases in efficiency, aircraft designers must look toward more unique solutions. The rotary horizontal tail configuration provides one such solution to reduce drag by roughly 6 percent without significantly affecting the lift. However, this drag reduction comes at the cost of a significant degradation in lateral stability and a near complete loss of directional stability. This degradation results in a Dutch roll mode with a reduced damping ratio and severely reduced natural frequency, which would be difficult to near impossible for a human pilot to correct or perform target tracking. Therefore, a digital control system is needed to control this aircraft configuration. A nonlinear MATLAB aircraft model was created for a conventional aircraft similar to the Cessna 172 and for a similar modified aircraft with a rotary horizontal tail. These models were linearized about the SLUF flight condition. First, a state-feedback LQR disturbance rejection controller was designed for the SLUF linearized model for both the conventional and modified aircraft. This controller stabilized all modes and greatly improved the Dutch roll characteristics of the modified model. The time domain performance of both controlled systems was nearly identical for disturbances in all axes. However, it was found that the modified model controller was significantly less robust than the conventional, especially with respect to A-matrix disturbances in specific channels. To equalize the robustness between the controlled systems, a controller was designed using a polytopic uncertainty guaranteed-cost LQR method. This method guarantees stability within defined upper and lower limits on the state-space matrices. This range was chosen to be ±50 percent in the eight channels of the A-matrix and three channels in the B-matrix that distinguished most between the conventional and modified systems. The conventional and modified systems controlled with these controllers had similar robustness qualities and could tolerate roughly equivalent A- and B-matrix perturbations in the selected channels while remaining stable. However, the time domain performance was significantly different. Both systems performed worse than the state-feedback LQR controlled systems, but the modified controlled system performed worse than the conventional in the lateral direction. The modified system had slower rise and settling times, greater overshoot and decay ratios, and did so at a higher control effort.

Ultimately, the rotary horizontal tail configuration promises an increase in aircraft range and can be stabilized and controlled using a digital controller. If the system dynamics uncertainties are small, the controlled rotary horizontal tail can match the time domain performance of an equivalent conventional aircraft. However, if system robustness must be designed for, the modified system will show a larger decrease in time domain performance for the same increase in robustness compared to the conventional system.

5.1 Future Efforts

Much more work must be done to make the rotary horizontal tail configuration a reality. Firstly, further work should be done to better understand the aerodynamic moments and forces on the rotary horizontal tail. This effort was limited by the relatively basic computational aerodynamic tools available, so future research should conduct complex computational fluid dynamics or wind tunnel studies to better approximate the system dynamics. Along with this, work will need to be done to assess the impact of the rotating horizontal tail on the inertia of the aircraft, which could be changing significantly over time as the tail rotates. With this data, a higher fidelity model can be created to aid in developing a pilot-in-the-loop controller with the purpose of making the configuration easy to fly for a human pilot. Finally, work must be done to determine how to mechanically support and actuate a rotary empennage. The results of this will determine if the aerodynamic benefits of this configuration are not cancelled by weight and complexity increases and will aid in the development of further controls research by providing rate and deflection limits and empennage weight and inertia.

BIBLIOGRAPHY

[1] Skyhawk model 172s: Specification and description, December 2012.

[2] Karl J. Aström and P.R. Kumar. Control: A perspective. *Automatica*, 50(1):3–43, 2014.

[3] D. Bernstein. Robust static and dynamic output-feedback stabilization: Deterministic and stochastic perspectives. *IEEE Transactions on Automatic Control*, 32(12):1076–1084, 1987.

[4] Christian R. Bolander, Austin Kohler, Douglas F. Hunsaker, David Myszka, and James J. Joo. Static trim of a fighter aircraft with a bio-inspired rotating empennage. *AIAA SCITECH 2023 Forum*, January 2023.

[5] Stephen Boyd, Laurent El Ghaoui, Eric Feron, and Venkataramanan Balakrishnan. *Linear Matrix Inequalities in System and Control Theory.* Society for Industrial and Applied Mathematics, 1 edition, 1994.

[6] S. Chang and T. Peng. Adaptive guaranteed cost control of systems with uncertain parameters. *IEEE Transactions on Automatic Control*, 17(4):474–483, 1972.

[7] Russel M. Cummings, William H. Mason, Scott A. Morton, and David R. McDaniel. *Applied Computational Aerodynamics: A Modern Engineering Approach.* Cambridge University Press, 1 edition, 2015.

[8] Andre Deperrois. Overview of the theoretical background in xflr5, March 2019.

[9] Andre Deperrois. Theoretical limitations and shortcomings of xflr5, March 2019.

[10] Andre Deperrois. Why does a plane fly: the inviscid flow potential flow, March 2019.

[11] Andre Deperrois. Why does an airfoil drag: the viscous problem, March 2019.

[12] Peter Dorato, Chaouki Abdallah, and Vito Cerone. *Linear-Quadratic Control: An Introduction.* Prentice-Hall, Inc, 1 edition, 1995.

[13] J. Doyle and G. Stein. Multivariable feedback design: Concepts for a classical/modern synthesis. *IEEE Transactions on Automatic Control*, 26(1):4–16, 1981.

[14] J. C. Doyle. Robustness of multiloop linear feedback systems. In *1978 IEEE Conference on Decision and Control including the 17th Symposium on Adaptive Processes*, pages 12–18, 1978.

[15] Mark Drela and Harold Youngren. Mit avl user primer - avl 3.36. 2022.

[16] S. K. Ghosh, T. K. Roy, M. A. H. Pramanik, and M. A. Mahmud. Lmi-based optimal linear quadratic controller design for multiple solar pv units connected to distribution networks. In *2021 IEEE Texas Power and Energy Conference (TPEC)*, pages 1–6, 2021.

[17] C. Harvey, V. B. Baliga, J. C. M. Wong, D. L. Altshuler, and D. J. Inman. Birds can transition between stable and unstable states via wing morphing. *Nature*, 603:648–653, 2022.

[18] Christina Harvey, Lawren L. Gamble, Christian R. Bolander, Douglas F. Hunsaker, James J. Joo, and Daniel J. Inman. A review of avian-inspired morphing for uav flight control. *Progress in Aerospace Sciences*, 132:100825, 2022.

[19] Christina Harvey, Lawren L. Gamble, Christian R. Bolander, Douglas F. Hunsaker, James J. Joo, and Daniel J. Inman. A review of avian-inspired morphing for uav flight control. *Progress in Aerospace Sciences*, 132:100825, 2022.

[20] Austin Kohler, Christian R. Bolander, Douglas F. Hunsaker, and James J. Joo. Linearized rigid-body static and dynamic stability of an aircraft with a bio-inspired rotating empennage. *AIAA SCITECH 2023 Forum*, January 2023.

[21] Eric Liner. Golden eagle soaring on a thermal, 2017.

[22] Robert A. McDonald and James R. Gloudemans. *Open Vehicle Sketch Pad: An Open Source Parametric Geometry and Analysis Tool for Conceptual Aircraft Design.*

[23] Tomas Melin. *User's guide and reference manual for Tornado*, 2000.

[24] Benjamin C. Moulton, Matthew W. Harris, Douglas F. Hunsaker, and James J. Joo. Evaluation of first-order actuator dynamics and linear controller for a bio-inspired rotating empennage fighter aircraft. *AIAA SCITECH 2024 Forum*, January 2024.

[25] Leonardo Nepomuceno, Éder A. Moura, Maurício A. Morales, Roberto G. Silva, and Luiz C. Góes. *An LQR-LMI Longitudinal Stability Augmentation System for a Subscale Fighter Aircraft with Variable Center of Gravity Position.*

[26] José Rivera Parga, Mark F. Reeder, Troy Leveron, and Ken Blackburn. Experimental study of a micro air vehicle with a rotatable tail. *Journal of Aircraft*, 44(6):1761–1768, 2007.

[27] Ian R. Petersen and Christopher V. Hollot. A riccati equation approach to the stabilization of uncertain linear systems. *Automatica*, 22(4):397–411, 1986.

[28] Luis Rodrigues. From lqr to static output feedback: a new lmi approach. In *2022 IEEE 61st Conference on Decision and Control (CDC)*, pages 4878–4883, 2022.

[29] Michael G. Safonov. Origins of robust control: Early history and future speculations. *IFAC Proceedings Volumes*, 45(13):1–8, 2012. 7th IFAC Symposium on Robust Control Design.

[30] Michael G. Safonov. Robust control: Fooled by assumptions. *International Journal of Robust and Nonlinear Control*, 28(12):3667–3677, 2018.

[31] Sigurd Skogestad and Ian Postlethwaite. *Multivariable Feedback Control Analysis and Design*. John Wiley and Sons, Ltd, 2 edition, 2005.

[32] Jialei Song, Jorn A. Cheney, Richard J. Bomphrey, and James R. Usherwood. Virtual manipulation of tail postures of a gliding barn owl (¡i¿tyto alba¡/i¿) demonstrates drag minimization when gliding. *Journal of The Royal Society Interface*, 19(187):20210710, 2022.

[33] G. Stein and M. Athans. The lqg/ltr procedure for multivariable feedback control design. *IEEE Transactions on Automatic Control*, 32(2):105–114, 1987.

[34] Brian L. Stevens and Frank L. Lewis. *Aircraft Control and Simulation*. John Wiley and Sons, Inc., 2 edition, 2003.

[35] Yifu Wang. The aerodynamics and stability analysis of a vertical tailless aircraft with rotary horizontal tail. Master's thesis, University of Washington William E. Boeing Department of Aeronautics and Astronautics, 2020.

[36] J. Willems. Least squares stationary optimal control and the algebraic riccati equation. *IEEE Transactions on Automatic Control*, 16(6):621–634, 1971.

[37] Peizhou Xia, Haochen Shi, Huiqing Wen, Qinglei Bu, Yihua Hu, and Yong Yang. Robust lmi-lqr control for dual-active-bridge dc–dc converters with high parameter uncertainties. *IEEE Transactions on Transportation Electrification*, 6(1):131–145, 2020.

[38] Thomas R Yechout, Steven L Morris, David E Bossert, Wayne F Hallgren, and James K Hall. *Introduction to Aircraft Flight Mechanics.* American Institute of Aeronautics and Astronautics, Inc., 2 edition, 2014.